Trapping of single atoms with single photons in cavity QED

A. C. Doherty, T. W. Lynn, C. J. Hood, and H. J. Kimble

Norman Bridge Laboratory of Physics 12-33,

California Institute of Technology, Pasadena, California 91125

Two recent experiments have reported the trapping of individual atoms inside optical resonators by the mechanical forces associated with single photons [Hood et al., Science 287, 1447 (2000), Pinkse et al., Nature 404, 365 (2000)]. Here we analyze the trapping dynamics in these settings, focusing on two points of interest. Firstly, we investigate the extent to which light-induced forces in these experiments are distinct from their free-space counterparts, and whether or not there are qualitatively different effects of optical forces at the single-photon level within the setting of cavity QED. Secondly, we explore the quantitative features of the resulting atomic motion, and how these dynamics are mapped onto experimentally observable variations of the intracavity field. Towards these ends, we present results from extensive numerical simulations of the relevant forces and their fluctuations, as well as a detailed derivation of our numerical simulation method, based on the full quantum-mechanical master equation. Not surprisingly, qualitatively distinct atomic dynamics arise as the coupling and dissipative rates are varied. For the experiment of Hood et al., we show that atomic motion is largely conservative and is predominantly in radial orbits transverse to the cavity axis. A comparison with the free-space theory demonstrates that the fluctuations of the dipole force are suppressed by an order of magnitude. This effect is based upon the Jaynes-Cummings eigenstates of the atom-cavity system and represents distinct physics for optical forces at the single-photon level within the context of cavity QED. By contrast, even in a regime of strong coupling in the experiment of Pinkse et al., there are only small quantitative distinctions between the potentials and heating rates in the free-space theory and the quantum theory, so it is not clear that a description of this experiment as a novel single-quantum trapping effect is necessary. The atomic motion is strongly diffusive, leading to an average localization time comparable to the time for an atom to transit freely through the cavity, and to a reduction in the ability to infer aspects of the atomic motion from the intracavity photon number.

I. INTRODUCTION

An exciting advance in recent years has been the increasing ability to observe and manipulate the dynamical processes of individual quantum systems. In this endeavor, an important physical system has been a single atom strongly coupled to the electromagnetic field of a high-Q (optical or microwave) cavity within the setting of cavity quantum electrodynamics (cavity QED). [1,2] Here the coupling frequency of one atom to a single mode of an optical resonator is denoted by g_0 (i.e., $2g_0$ is the one-photon Rabi frequency), with the regime of strong coupling defined by the requirement that $g_0 \gg (\gamma, \kappa)$, where γ is the atomic decay rate to modes other than the cavity mode and κ is the decay rate of the cavity mode itself. In this circumstance, the number of photons required to saturate an intracavity atom is $n_0 \sim \gamma^2/g_0^2 \ll 1$ and the number of atoms required to have an appreciable effect on the intracavity field is $N_0 \sim \kappa\gamma/g_0^2 \ll 1$ [3].

Although there have been numerous laboratory advances which demonstrate the effect of strong coupling on the *internal* degrees of freedom of an atomic dipole coupled to the quantized cavity field (i.e., $g_0 \gg \kappa, \gamma$), the consequences of strong coupling for the *external*, atomic center-of-mass motion with kinetic energy E_k have only recently been explored experimentally [4–9]. In a regime of strong coupling for the *external* degrees of freedom, $g_0 > E_k/\hbar$, a single quantum is sufficient to profoundly alter the atomic center-of-mass (CM) motion, as an atom moves through a region of spatially varying coupling coefficient $g(\vec{r}) = g_0\psi(\vec{r})$ [*e.g.*, as arises in the Gaussian mode of a Fabry-Perot cavity, $\psi(\vec{r})$].

Perhaps most strikingly, the spatial variation of the cavity mode can lead to a confining potential sufficient to trap an atom within the cavity mode even for a single quantum of excitation of the atom-cavity system, as first discussed in the work of Refs. [10,11]. This is illustrated in Fig. 1, which shows the the possibility for trapping by excitation to the lower component $|-\rangle$ in the Jaynes-Cummings manifold of eigenstates. Modifications of the atomic CM dynamics can in turn significantly alter the cavity field. This situation is very different from the usual case for trapped atoms or ions in fixed external potentials, in that here the confining field and the atomic motion can be strongly interacting, in which case the overall state of the system must be determined in a self-consistent fashion.
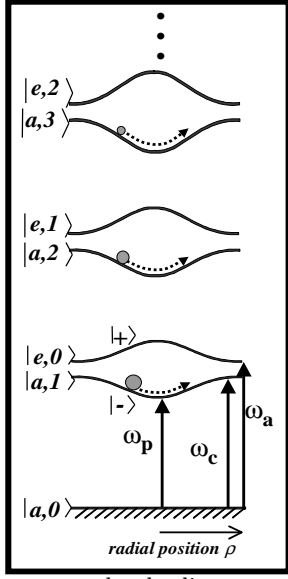
FIG. 1. The energy-level diagram for the coupled atom-cavity system, as a function of the atom's radial position ρ. When the atom is near the cavity center, driving at frequency ω_p populates the state $|-\rangle$ to trap the atom. Here $\omega_{(p,c,a)} = \omega_{(probe,cavity,atom)}$ of the text.

The experimental requirements to investigate strong coupling for both the *internal* and *external* degrees of freedom are stringent [namely, $g > (E_k/\hbar, \gamma, \kappa)$], and have required the integration of the techniques of laser cooling and trapping with those of cavity QED, as was initially achieved in 1996 [12] and as illustrated in Fig. 2. Mechanical effects due to strong coupling with single quanta were first observed in 1998 [4], in an experiment with peak coupling energy $\hbar g_0 \simeq 5$ mK and with initial atomic kinetic energy $E_k \simeq 400\mu$ K.

Following this theme, two groups recently reported trapping of single atoms with intracavity fields at the single-photon level, beginning with the work of Ref. [5] and culminating in that of Refs. [7,8]. That such trapping might be possible in these experiments is indicated by the fact that the ratio R of initial atomic kinetic energy E_k to the coherent coupling energy $\hbar g_0$, $R \equiv E_k/\hbar g_0$, is less than unity. For the work in Refs. [5,7], $R \simeq 0.06$, while for that in Ref. [8] $R \simeq 0.27$. Although these ratios are indicative of the possibility of trapping with single quanta in cavity QED, the actual forces and confining potentials are somewhat more complex to analyze, as we shall see. Moreover, beyond providing single-quantum forces sufficient for atomic localization, strong coupling also means that the presence of one atom can significantly modify the intracavity field, thereby providing a means to track atomic motion by way of the light emerging from the cavity.

To understand the basic scheme for trapping of single atoms with single quanta in cavity QED, consider the energies $\hbar\beta_\pm$ for the first excited states $|\pm\rangle$ of the atom-cavity system. Along the radial direction $\rho = \sqrt{y^2 + z^2}$ and for optimal x (standing-wave) position, $\beta_\pm(\rho)$ has

the spatial dependence indicated in Fig. 1, which neglects dissipation. The ground state of the atom-cavity system is $|a,0\rangle$; the atom is in its ground state a, and there are no photons in the cavity. For weak coupling (atom far from the cavity mode center), the first two excited states are that of one photon in the cavity and the atom in the ground state, $|a,1\rangle$, and of the atom in the excited state e with no photons in the cavity, $|e,0\rangle$. These two states are separated by an energy $\hbar\Delta_{ac}$, where $\Delta_{ac} \equiv \omega_{cavity} - \omega_{atom}$ is the detuning between the "bare" (uncoupled) atom and cavity resonances.

FIG. 2. Experimental schematic for the case of Hood *et al.* Atoms are captured in a magneto-optical trap (MOT), and dropped or launched through a high-finesse optical cavity. A single atom (trace with arrow) transiting the cavity mode alters the measured transmission of a probe beam through the cavity. In the experiment of Pinkse *et al.*, rubidium atoms are captured in a MOT below the cavity and launched upward through it.

As an atom enters the cavity along ρ it encounters the spatially varying mode of the cavity field, and hence a spatially varying interaction energy $\hbar g(\vec{r})$, given by $g(\vec{r}) = g_0 \cos(kx/) \exp(-(y^2 + z^2)/w_0^2)$ ($k = 2\pi/\lambda$). The bare states map via this coupling to the dressed states $|\pm\rangle$ shown in the figure, with energies

$$\beta_\pm = \frac{\omega_{atom} + \omega_{cavity}}{2} \pm [g(\vec{r})^2 + \frac{\Delta_{ac}^2}{4}]^{1/2}. \qquad (1)$$

Our interest is in the state $|-\rangle$; the spatial dependence of the energy $\hbar\beta_-(\vec{r})$ represents a pseudopotential well that can be selectively populated by our choice of driving field $\mathcal{E}_{probe}(t)$ and Δ_{probe} to trap the atom, as first suggested by Parkins [13]. The system is monitored with a weak probe beam as an atom enters the cavity mode; detection of an atom transit signal triggers an increase in driving strength to populate the state $|-\rangle$ and trap the atom. Because the experiments in the optical domain have atomic and cavity decay times $(\kappa^{-1}, \gamma^{-1})$ that are small compared to the time τ for motion through the cavity field, the atom-cavity system must be continually re-excited by way of $\mathcal{E}_{probe}$, thereby providing an effective pseudopotential on time scales δt such that $(\kappa^{-1}, \gamma^{-1}) \ll \delta t \ll \tau$.

Although a full theory based on the preceding discussion is *sufficient* to provide detailed agreement with the experimental observations of Refs. [5,7,8] (as we shall show in subsequent sections), it is reasonable to ask to what extent such a theory based on the interactions in cavity QED is *necessary*. In particular, it might well be that the well-established theory of laser cooling and trapping in free space [14] could provide an adequate description of the potentials and heating rates, with the cavity merely providing a convenient means for attaining a strong drive field. With respect to the experimental results of Pinkse *et al.* (Ref. [8]), we find that this is in fact largely the case; there are only small quantitative distinctions between the free-space theory and the appropriate

quantum theory. One interesting feature to note in this experiment is enhanced cooling of the atomic motion relative to the parameters of Hood *et al.* [7]. This effect, which enables trapping in this parameter regime, arises through cavity-mediated cooling [15,16]. For these parameters, the average localization time from simulations is extended by 75% relative to the equivalent free-atom signal; both these times are shorter than the time for an atom to transit freely through the cavity.

By contrast, in the regime of the experiment of Hood *et al.* (Ref. [7]), the cavity QED interactions result in a strong suppression of dipole heating along the cavity axis relative to the free-space theory, which has a strong effect on both the duration and character of the observed atom transits. In the cavity QED setting it becomes possible to create a potential deep enough to trap an atom without simultaneously introducing heating rates that cause rapid escape from that potential. For these parameters, the average experimentally observed localization time is a factor of 3.5 longer than the equivalent free-atom average. The results of extensive numerical simulations of trapping times and radial oscillation frequencies, and their validation by way of comparisons to experimentally measured distributions, demonstrate the essential role of the single-photon trapping mechanism in the experiment of Ref. [7]. At root is the distinction between the nonlinear response of an atom in free space and one strongly coupled to an optical cavity. For these experimental parameters, the eigenvalue structure of Fig. 1 leads to profound differences between the standard theory of laser cooling and trapping, and the extension of this theory to the regime of strong coupling in cavity QED.

Note that prior experiments in our group have confirmed that the full quantum treatment of the one-atom master equation in cavity QED is required for a description of the dynamics associated with the internal degrees of freedom for a single atom in an optical cavity in the regime $g > (\gamma, \kappa)$. These experimental confirmations come by way of measurements of the nonlinear susceptibility for the coupled system in settings close to that for the experiment of Ref. [7] [4,5,17]. A principal goal of this paper is to investigate the extent to which a theory of atomic motion within the setting of cavity QED is likewise a *necessary* component in describing the center-of-mass dynamics for the experiments of Refs. [7,8].

A second goal is to examine the related question of the extent to which inferences about atomic motion within the cavity can be drawn from real-time observations of the cavity field, either via photon counting [8] or heterodyne detection [7] of the cavity output. The interactions in cavity QED bring an *in principle* enhancement in the ability to sense atomic motion beyond that which is otherwise possible in free space. Stated more quantitatively, the ability to sense atomic motion within an optical cavity by way of the transmitted field can be characterized by the optical information $I = \alpha g_0^2 \Delta t/\kappa \equiv \alpha \mathcal{R} \Delta t$, which, roughly speaking, is the maximum possible number of photons that can be collected as signal in time Δt with efficiency α as an atom transits between a region of optimal coupling g_0 and one with $g(\vec{r}) \ll g_0$. A key enabling aspect of the experiments in Refs. [7,8] is that $\mathcal{R} = g_0^2/\kappa \gg (\kappa, \gamma)$, leading to information about atomic motion at a rate that far exceeds that from either cavity or spontaneous decay (as in fluorescence imaging). In practice, for detection strategies employed experimentally, information is extracted at a somewhat lower rate. For example, in the experiment of Hood et al. [7], the photon count rate would be $(2.7 \times 10^7/\text{s})$ (including the overall escape and detection efficiency $\alpha \approx 0.15$), while for the experiment of Pinkse et al. [8] it is $(2.2 \times 10^6/\text{s})$ (including an estimated overall escape and detection efficiency $\alpha \approx 0.11$) [18]. For time scales $\Delta t \sim 10\mu$ s as relevant to the following discussion, atomic motion through the spatially varying cavity mode leads to variations in the transmitted field that can be recorded with a high signal-to-noise ratio, namely, a signal of 2.7×10^2 photons for the experiment of Hood et al. and 2.2×10^1 for that of Pinkse et al., where each is calculated for an intracavity field strength of one photon.

The value of the optical information itself does not tell the complete story. For cavity QED experiments like those considered here, one records either the sequence of photoelectric counts or the heterodyne current versus time, from which necessarily only limited inferences about atomic motion can be drawn. However, if center-of-mass dynamics (i.e., axial and radial motions) occur on well-separated time scales, then it is reasonable to suggest that appropriate signal processing techniques could extract information about these motions from the single time sequence of the photocurrent $i(t)$. Such processing could presumably occur in real time if $\alpha \mathcal{R}$ is much faster than the rates for radial and axial motion [e.g., the oscillation frequencies (f_r, f_a) in a potential well, with $f_r \ll f_a$]. Unfortunately, in neither experiment [7,8] is $\alpha \mathcal{R}$ large enough to resolve the axial dynamics directly, so the task of disentangling the radial and axial motion signals becomes more difficult, and theoretical simulations of the experiment become useful in understanding the nature of the observed transmission signals.

This difficulty arises in the experimental regime of Pinkse et al. [8]. For these parameters, axial heating leads to frequent bursts of large-amplitude motion along the cavity axis, with envelopes extending over time scales comparable to those for radial motion. Consequently, at experimental bandwidths (averaging times), both types of motion give rise to qualitatively similar modulations in the measured transmission signal. Furthermore, motion in the radial direction has a strong diffusive component, giving rise to a wide spread of time scales for radial motion. Our simulations discussed in Sec. V suggest that for these parameters, short-time-scale modulations ($\lesssim 300~\mu$s) tend to be mostly due to bandwidth averaging over axial motion, while longer ($\gtrsim 500~\mu$ s) variations such as presented in Fig. 2 of Ref. [8] typically reflect radial motion, though these long-time-scale variations are

generally modified in amplitude by the presence of axial motion. Modulations on intermediate time scales appear ambiguous in their dynamical origin.

By contrast, as shown in Ref. [7], for the parameters of Hood et al. atoms are well localized along the standing-wave direction throughout most of the trapping interval, with axial motion giving rise to negligible signal until finally rapid axial heating leads to atomic escape. Consequently, observed variations in the photocurrent $i(t)$ are simpler than those of Ref. [8], and directly yield the radial atomic position. Furthermore, in this experiment the radial oscillation frequency is large compared to the spontaneous emission heating rate, meaning that the resulting atomic motion is largely conservative (rather than diffusive) in nature, taking place in a known potential (as demonstrated both experimentally and by way of numerical simulation). Hence, from $i(t)$ it becomes possible to make detailed inferences about the radial motion, even to the point of real-time observations of the anharmonic motion of a single atom and of the reconstruction of actual atomic trajectories.

The structure of the paper is as follows. Following this introduction, in Sec. II we present a detailed description of our theoretical model and its use for the implementation of numerical simulations. Section III compares effective potentials and momentum diffusion rates derived for the two experiments, along with their analogs for the hypothetical case of an equal-intensity free-space trap. These calculations explore the distinction between quantum and classical, and also give insight into the nature of atomic motion expected in both experiments. Sample simulated trajectories are presented for both cases. In Sec. IV we present experimental and simulation results for the case of Hood et al., which serve both to verify the simulations and also to demonstrate important features of the resulting motion. Sec. V gives the application of the same tools to analyze the experiment of Pinkse et al.; we see that standing-wave motion and diffusive radial motion complicate the correlation between atomic position and detected field in this case. Finally, axial motion is explored in more depth, and Fourier analysis of our simulations show that oscillations of comparable amplitude and frequency should be visible for both atoms confined (but heated) within a well, and atoms skipping along the standing wave.

Principal findings

The theoretical treatment and numerical simulation of the motion of a single atom strongly coupled to an optical cavity, as described in Sec. II, lead to a surprisingly rich range of often qualitatively different dynamics. The motion may be essentially conservative and tightly confined around antinodes of the standing wave, or essentially dissipative and diffusive and involve interesting flights between different potential wells of the standing wave. Indeed we find that the existing experimental results of Hood et al. and Pinkse et al. exemplify these very different dynamical regimes. Key features of the atomic motion in both experimental regimes are addressed as follows:

Figures 3–5 and their associated discussion in Sec. III elucidate the nature of the trapping potential and momentum diffusion in an optical cavity as opposed to a free space standing wave. In particular we find that, even when the atom-cavity system is strongly coupled and driven such that it has a mean intracavity photon number of roughly 1, the trapping potential and momentum diffusion may be only slightly different from those in a free-space standing wave, and in fact this is the case for the parameters of Pinkse et al. On the other hand, for the parameters of Hood et al. the usual fluctuations of the dipole force along the standing wave are suppressed by an order of magnitude, which to our knowledge represents qualitatively new physics for optical forces at the single-photon level within the context of cavity QED. We show that in the parameter regime of Pinkse et al. the heating rates are such that the atom could be expected to gain energy equal to a significant fraction of the total trapping potential during a single motional oscillation period for both axial and radial motion. By this measure the heating rates in the experiment of Hood et al. are much slower, indicating more nearly conservative motion, and this could be expected to have a profound effect on the qualitative nature of the dynamics in the two experiments.

Figures 6 and 7 and the corresponding text in Sec. III present simulated transits for both experiments, and discuss the qualitative features of atomic dynamics in both cases. For the parameter regime of Hood al., conservative radial motion dominates diffusion and standing-wave motion, with atomic trajectories localized at peaks of a single standing-wave antinode. Atoms trapped with the mean trapping time execute several radial orbits. The eventual escape is typically due to heating along the cavity axis. By contrast, for the experiment of Pinkse et al., a trajectory of typical duration, as in Fig. 7(a), does not experience a complete radial orbit and in fact resembles a scattering event, with a large contribution from radial diffusion as well. For these events the observed localization time is comparable to the time for free flight through the cavity. Axially the simulations show that in longer duration transits the atom frequently skips between wells of the standing-wave potential due to repeated heating and recooling.

Section IV, with Figs. 8–10, presents a more detailed and quantitative investigation of trapping and motional dynamics for the experiment of Hood et al. The ability of our simulations to closely reproduce the mean trapping times observed in the experiment provides evidence of their accuracy and utility. As illustrated in Fig. 9, the triggering strategy leads to significant modifications of the distribution of residence times within the cavity. The essentially conservative nature of the dynamics and

the strong axial confinement make it possible to confidently ascribe oscillations in the transmitted intensity to radial motion of the atom. As shown in Fig. 10, the experimentally observed oscillations are consistent with the calculated potential. The conservative nature of the motion is further confirmed by the separation of orbital periods by angular momentum that is also apparent in this figure.

Section V, with Figs. 11–15, presents a detailed analysis of trapping and motional dynamics for the experiment of Pinkse et al. Again, our simulations are sufficient to reproduce the reported mean localization time. In this case, the triggering strategy leads to relatively minor modifications of the distribution of residence times for an atom within the cavity. In this case the dissipative nature of the evolution is significant; essentially no long-term localization is observed if the sign of the friction coefficient is reversed, whereas this has little effect in the parameter regime of Hood et al. These largely dissipative and diffusive motional dynamics are found to have significant effect on the information about the motion that is available in the transmitted field. For those events with a long localization time, the axial motion of the atom is repeatedly heated and cooled, resulting in slow variations in envelope of the amplitude of the rapid oscillations of the transmitted light. The time scale of these variations is comparable to that for radial motion of the atom. There are thus no unambiguous signatures for radial motion and only longer time scale excursions of the atom in the radial potential lead to variations of the output field that may be confidently ascribed to the radial motion. Likewise, although information about axial motion is also available in the output light, we find that it is in general difficult to distinguish large oscillations in a single well of the axial potential from free flight over several wells as attempted in Ref. [8].

II. THEORETICAL MODEL AND NUMERICAL SIMULATIONS

In this section we outline the derivation from the full quantum-mechanical master equation of the "semiclassical model" for the atomic motion used in Ref. [7]. It turns out that this model is able to reproduce the experimental observations very accurately. Note that here the term "semiclassical" refers to approximations with respect to the atomic center-of-mass motion, and not to the internal degrees of freedom, for which the full quantum character is retained. This situation should not be confused with the semiclassical theory of cavity QED for which expectation values of field operators $\hat{O}_{field}$ and atomic operators $\hat{O}_{field}$ are assumed to factorize, $\langle \hat{O}_{field} \hat{O}_{atom} \rangle = \langle \hat{O}_{field} \rangle \langle \hat{O}_{atom} \rangle$; no such approximation is made here. To distinguish these two cases, we introduce the term *quasiclassical* for the case of atomic motion.

The validity of the quasiclassical model depends on a separation of time scales between the atomic motion and the cavity and internal atomic dynamics. We adapt the work of Dalibard and Cohen-Tannoudji [14] to the situation of a quantized cavity mode. A similar derivation in the bad-cavity limit appears in [19]. The details of the derivation are essentially unchanged from free space, since the terms of the master equation which refer to the dynamics of the cavity have no explicit dependence on the operators describing the atomic motion. However, we do find conditions for the validity of the approximation for this system which depend on the properties of the cavity. Finally, we describe in more detail the numerical simulations of the resulting model first presented in Ref. [7]. These simulations are of the kind discussed in Refs. [20,21].

An analytical calculation of force, momentum diffusion and friction coefficients for the quasiclassical model of atomic motion in the low driving limit was derived by Horak and co-workers [15,22], who found a regime in which the steady-state temperature scaled as the cavity decay rate. This allows cooling of the atom below the Doppler limit, so long as the cavity can be made to have lower loss than the atom. However, the parameters of Refs. [7,8] are very far from this low driving limit. Hence we employ numerical techniques based on solving the appropriate master equations by expansions in terms of Fock states of the cavity field [23]. Note that a very early contribution developed a different theoretical framework and numerical scheme for calculating the force and friction (but not the momentum diffusion) of an atom in a cavity (or "colored vacuum") [24,25]. Very recently, Vuletic and Chu [16] found cavity-mediated cooling in a slightly different regime to that considered by Horak et al.

A. Model of atom-light interaction in a cavity

The Hamiltonian for a two-level atom interacting with a single mode of the electromagnetic field in an optical cavity using the electric dipole and rotating-wave approximations (in the interaction picture with respect to the laser frequency) is

$$H = \frac{\vec{p}^2}{2m} + \hbar(\omega_{atom} - \omega_{probe})\sigma^\dagger\sigma + \hbar(\omega_{cavity} - \omega_{probe})a^\dagger a$$
$$+ \hbar g(\vec{r})(a^\dagger\sigma + \sigma^\dagger a) + \hbar\left(\mathcal{E}a^\dagger + \mathcal{E}^*a\right). \tag{2}$$

This is the familiar Jaynes-Cummings Hamiltonian modified to take into account the external degrees of freedom of the atom and the spatial variation of the cavity mode. The first term is the kinetic energy of the atom, and the next two terms are the energy in the internal state of the atom and the cavity excitation. The fourth term describes the position-dependent interaction of the cavity mode and the atomic dipole. It is important to note

that $\vec{r}$ and $\vec{p}$ are operators. Thus, for example, the exact strength of the coupling between the atomic internal state and the cavity field depends on the shape of the atomic wave packet, which is in turn determined by the mechanical effects of the cavity field. Some implications of this Hamiltonian are considered in detail by Vernooy and Kimble [26]. The Hamiltonian has been written in terms of cavity and dipole operators that rotate at the frequency of the probe field ω_{probe}. The real atomic transition (cesium in Ref. [7] and rubidium in Ref. [8]) in fact involves several degenerate magnetic sublevels, but we assume that the cavity is driven by circularly polarized light and that the atom is optically pumped such that it occupies an effective two-level system described by the dipole operator σ with the quantization axis along x.

Dissipation in the system is due to cavity losses and spontaneous emission. By treating modes external to the cavity as a heat reservoir at zero temperature in the Born, Markov, and rotating-wave approximations, it is possible to derive the standard master equation for the density operator ρ of the system [14,27] as

$$
\begin{aligned}
\frac{d\rho}{dt} = &\frac{-i}{\hbar}[H, \rho] + \kappa(2a\rho a^\dagger - a^\dagger a\rho - \rho a^\dagger a) \\
&+ \frac{3\gamma}{4\pi} \int d^2\hat{\mathbf{k}} S(\hat{\mathbf{k}} \cdot \hat{\mathbf{x}}) \exp(-ik\hat{\mathbf{k}} \cdot \mathbf{r}) \sigma\rho\sigma^\dagger \exp(ik\hat{\mathbf{k}} \cdot \mathbf{r}) \\
&- \gamma(\sigma^\dagger\sigma\rho + \rho\sigma^\dagger\sigma).
\end{aligned} \tag{3}
$$

The third and fourth terms describe the effect of spontaneous emission on the atomic motion including the momentum kick experienced by the atom as a result of the spontaneous emission. The unit vector $\hat{\mathbf{k}}$ is the direction of an emitted photon. The pattern of dipole radiation is accounted for by the angular factor $S(\hat{\mathbf{k}} \cdot \hat{\mathbf{x}}) = \left[1 + (\hat{\mathbf{k}} \cdot \hat{\mathbf{x}})^2\right]/2$ [28].

B. Quasiclassical motion of the center of mass

It is possible to eliminate the internal and cavity dynamics adiabatically in favor of the slower dynamics of the motional state in parameter regimes of direct relevance to current experiments. Intuitively, for the quasiclassical approximation to work, the state of the atom needs to be sufficiently localized in position and momentum on the scales important to the problem so that it can be thought of as a classical particle. The conditions for adiabatically eliminating the internal and cavity dynamics roughly correspond to this idea. It turns out that it is necessary first that exchanges of momentum with either the cavity field or by spontaneous emission into free space should result in momentum kicks that are small compared with the momentum spread Δp of the atomic Wigner function, thus

$$
\varepsilon_1 \simeq \hbar/\Delta p \ll 1. \tag{4}
$$

For an atom which is in a minimum uncertainty state with respect to the position-momentum Heisenberg inequality this requires that the state is localized to better than a wavelength. The atomic motional state will in general be a mixture allowing the position spread to be broader. However, this requirement means that the motional state can be thought of as a probabilistic mixture of pure states localized to within a wavelength, and so places a limit on the coherence length of the motional state [29]. Second it is important that the range of Doppler shifts of the atom due to its momentum spread is small compared to the atomic and cavity linewidths, thus

$$
\varepsilon_2 \simeq k\Delta p/m\gamma \simeq k\Delta p/m\kappa \ll 1. \tag{5}
$$

In this paper it will be assumed that the root-mean-square atomic momentum obeys this inequality, thus making a low velocity approximation, but the arguments here can in fact be generalized to arbitrary mean velocities of the atom [30]. The Heisenberg inequality means that this also requires a minimum position spread of the atom

$$
\Delta r \gg \hbar k/m\gamma, \hbar k/m\kappa. \tag{6}
$$

These criteria are a simple generalization of the situation for laser cooling in free space which can be imagined as the situation $\kappa \to \infty$. The consistency of these conditions, which effectively put lower and upper limits on the atomic momentum spread, requires that

$$
\frac{\hbar^2 k^2/2m}{\hbar\gamma} \ll 1, \quad \frac{\hbar^2 k^2/2m}{\hbar\kappa} \ll 1. \tag{7}
$$

The first of these conditions is well known for laser cooling in free space—the requirement that the recoil energy of the atomic transition be much lower than the Doppler energy, which effectively controls the limiting temperature of the laser cooling. This condition is well satisfied for heavy atoms such as cesium and rubidium and the optical transitions employed in cavity QED experiments considered here. The analogous condition brought about by the cavity dynamics requires that the recoil energy associated with exchanging excitation with the cavity field is much smaller than the energy width of the cavity resonance. Just as the first criterion implies that the atom still be in resonance with a driving field at its transition frequency after spontaneously emitting, the second criterion implies that absorbing or emitting a photon from the cavity will leave the atom near the cavity resonance. In the experiments of Refs. [5,7,8], $\kappa \sim \gamma$, so that this second criterion does not place a stronger restriction on the validity of the approximations than the free-space limit. However, it is important to note that the design of the cavity, as well as the atom and transition that are chosen, now has an effect on the validity of the approximation. It would be possible, for example, to change the cavity length in such a

way that the system moves from a regime in which the quasiclassical treatment is appropriate into one in which it is not. In practice for cold atoms cooled to roughly the Doppler limit ($\Delta p^2/2m \sim \hbar\gamma, \hbar\kappa$) it will be the case that $\varepsilon_1 \simeq \varepsilon_2 \sim \sqrt{(\hbar^2 k^2/2m)/\hbar\gamma}, \sqrt{(\hbar^2 k^2/2m)/\hbar\kappa}$, and so a consistent expansion should be to equal order in these small parameters.

The derivation of Ref. [14] may be applied to our problem, and proceeds by transforming the master equation [Eq. 3] into an evolution equation for a Wigner operator,

$$W(\vec{r}, \vec{p}, t) = \frac{1}{h^3} \int d^3\vec{u} \langle \vec{r} + \tfrac{1}{2}\vec{u} | \rho | \vec{r} - \tfrac{1}{2}\vec{u} \rangle \exp(-i\vec{p}\cdot\vec{u}/\hbar),$$
(8)

describing the complete state of the system. An approximate Fokker-Planck equation for the Wigner function describing the motional degrees of freedom alone is found by writing this equation as a Taylor expansion in terms of the small parameters ε_1 and ε_2, and truncating that expansion at third order. The force operator is defined as the gradient of the atom-cavity coupling

$$\vec{F}(\vec{r}) = -\hbar g_0 \vec{\nabla}\psi(\vec{r})(a^\dagger \sigma + \sigma^\dagger a).$$
(9)

It is possible to show that the Fokker-Planck equation for the atomic Wigner function f takes the form

$$\frac{\partial}{\partial t}f + \frac{\vec{p}}{m}\cdot\frac{\partial}{\partial \vec{r}}f = -\vec{\phi}(\vec{r})\cdot\frac{\partial}{\partial \vec{p}}f + \sum_{ij} D_{ij}\frac{\partial^2}{\partial p_i \partial p_j}f + \hbar^2 k^2 \gamma \langle \sigma^\dagger \sigma \rangle_{\rho_s} \sum_{ij} E_{ij}\frac{\partial^2}{\partial p_i \partial p_j}f + \sum_{ij} \eta_{ij}\frac{\partial^2}{\partial p_i \partial r_j}f + \sum_{ij} \Gamma_{ij}\frac{\partial}{\partial p_i}(p_j f).$$
(10)

The quantities appearing in the Fokker-Planck equation can be calculated from the master equation for the internal and cavity degrees of freedom alone that is obtained by setting $\vec{r}$ to some real number value $\vec{r}_0$, and disregarding the kinetic-energy term. We define $\rho_s(\vec{r})$ as the steady state of this master equation, with the steady-state expectation value of the arbitrary operator c given by $\langle c \rangle_{\rho_s} = \mathrm{Tr}(c\rho_s(\vec{r}))$. The parameters appearing in the Fokker-Planck equation can then be expressed as follows:

$$\vec{\phi}(\vec{r}) = \mathrm{Tr}\left[\vec{F}(\vec{r})\rho_s(\vec{r})\right],$$

$$D_{ij} = \int_0^\infty d\tau \left[\frac{1}{2}\langle F_i(\tau) F_j(0) + F_j(0) F_j(\tau)\rangle_{\rho_s} - \phi_i\phi_j\right],$$

$$E_{ij} = \frac{3}{8\pi}\int d^2\hat{k} S(\hat{k}\cdot\hat{x})\hat{k}_i\hat{k}_j,$$

$$\eta_{ij} = \frac{1}{m}\int_0^\infty d\tau\tau \left[\frac{1}{2}\langle F_i(\tau) F_j(0) + F_j(0) F_j(\tau)\rangle_{\rho_s} - \phi_i\phi_j\right],$$

$$\Gamma_{ij} = \frac{i}{m\hbar}\int_0^\infty d\tau\tau \langle[F_i(\tau), F_j(0)]\rangle_{\rho_s}.$$

Simple integrations give $E_{xx} = 2/5$ and $E_{yy} = 3/10 = E_{zz}$ and all other components of E are zero. Excepting the different definition of the force operator $\vec{F}$, these are the expressions that can be derived in case of a free-space light field [14]. However, it is important to bear in mind the extra conditions on the validity of the adiabatic elimination. The master equation [Eq. 3] means that the force expectation values and correlation functions can be very different from those that are calculated in free space. In practice, the contribution from the parametric tensor η is often smaller than that from the diffusion tensor D by a factor of order ε, and is usually disregarded in treatments of free-space laser cooling [14].

Thus, as assumed in earlier work, calculating the quasiclassical motion of the atom in a cavity field only requires that the force and its correlation function be evaluated for the full atom-cavity master equation. Such prior treatments assumed that the atom is motionless;

however, they can be extended to atoms moving at some velocity under the same conditions [30,31]. The diffusion coefficients may be found by first calculating the correlation functions via the quantum regression theorem and numerical integration, or directly via matrix-continued fraction techniques [30,31]. A matrix-continued fraction calculation requires that the field mode be periodic, and as such it only works along the standing-wave axis of the cavity mode. In directions perpendicular to this, the calculation of correlations from the master equation is essentially the only option if the atom is not slowly moving.

C. Stochastic simulations of the quasiclassical model

It is possible to recast the Fokker-Planck equation of Eq. 10 into a simple set of stochastic equations which

describe atomic trajectories in the cavity field. These equations can be used to gain intuition about the atomic motion and how it is affected by mechanical forces. The diffusion and friction tensors can be rewritten using the definition of the force operator [Eq. (9)]

$$
\begin{aligned}
D &= \hbar^2 g_0^2 \left[\vec{\nabla}\psi(\vec{r})\right]\left[\vec{\nabla}\psi(\vec{r})\right]^T \int_0^\infty d\tau \left[\frac{1}{2}\left\langle \Phi\left[\tau\right]\Phi\left[0\right] + \Phi\left[0\right]\Phi\left[\tau\right]\right\rangle_{\rho_s} - \left\langle\Phi\right\rangle_{\rho_s}^2\right] \\
&= \hbar^2 g_0^2 \xi(\vec{r}) \left[\vec{\nabla}\psi(\vec{r})\right]\left[\vec{\nabla}\psi(\vec{r})\right]^T,
\end{aligned}
\tag{11a}
$$

$$
\begin{aligned}
\Gamma &= \frac{i}{m}\hbar g_0^2 \left[\vec{\nabla}\psi(\vec{r})\right]\left[\vec{\nabla}\psi(\vec{r})\right]^T \int_0^\infty d\tau\, \tau \left\langle\left[\Phi\left[\tau\right],\Phi\left[0\right]\right]\right\rangle_{\rho_s} \\
&= \frac{\hbar g_0^2}{m}\chi(\vec{r}) \left[\vec{\nabla}\psi(\vec{r})\right]\left[\vec{\nabla}\psi(\vec{r})\right]^T,
\end{aligned}
\tag{11b}
$$

where $\Phi = a^\dagger\sigma + \sigma^\dagger a$. Writing the parameters of the quasiclassical model in this form relies on the approximation that the atom is slowly moving, namely, that it does not move a significant fraction of a wavelength during a cavity or atomic lifetime. Note that the functions ξ and χ depend on position only through the coupling $g = g_0\psi$. They can be calculated efficiently by finding D_{xx} and Γ_{xx} using matrix-continued fractions, and then dividing off the gradient factors. A matrix-continued fraction technique cannot be used to find the other components of the momentum diffusion or the friction tensors directly, since the field mode is not periodic across the Gaussian profile of the mode.

It is now straightforward to convert the Fokker-Planck equation for the Wigner function into an equivalent set of Itô stochastic differential equations. The resulting (Itô) equations are [32]

$$
d\vec{x} = \frac{1}{m}\vec{p}\,dt,
\tag{12a}
$$

$$
\begin{aligned}
d\vec{p} = &-\hbar g_0\langle\Phi\rangle\vec{\nabla}\psi\, dt - \frac{\hbar g_0^2}{m}\chi(\vec{r})\left(\vec{p}\cdot\vec{\nabla}\psi\right)\vec{\nabla}\psi \\
&+2\hbar g_0\sqrt{\xi(\vec{r})}\vec{\nabla}\psi\, dW_1 + 2\hbar k\gamma\sqrt{\langle\sigma^\dagger\sigma\rangle}\sqrt{E}\,d\vec{W}.
\end{aligned}
\tag{12b}
$$

The Wiener increment dW_1 has the usual properties, in particular $dW_1^2 = dt$. The vector $d\vec{W}$ is a vector of three such increments. The terms in the equation for the momentum are the mean radiative force, its first-order dependence on momentum, and its fluctuations due to the atom-cavity system and due to the coupling to free space, respectively. These equations depend on the quantities $\langle\Phi\rangle, \chi, \xi$ and $\langle\sigma^\dagger\sigma\rangle$, which are functions of position through g only. A straightforward simulation of these equations only needs to store ordered look-up tables of these quantities for given values of g, rather than for all possible values of $\vec{r}$. All of the other quantities that appear, including g, are simple functions of $\vec{r}$ and $\vec{p}$. At each time step the algorithm searches the look-up table for the current value of g, starting from the previous value, and reads off the current values of $\langle\Phi\rangle, \chi, \xi, \langle\sigma^\dagger\sigma\rangle$. A linear interpolation for the two closest values of g was used, but more sophisticated interpolation schemes could be implemented. Since g will not change by a large amount in any one timestep the search can be very efficient; a routine from Ref. [33] was used for this. In the low-velocity limit of the quasiclassical theory, these stochastic differential equations describe all the motional dynamics of the atom inside the cavity. The term proportional to η_{ij} leads to correlations between the atomic position and momentum. The effect of η_{ij} is typically small compared to friction and diffusion and has been ignored for the moment as is common practice in free-space standing waves. Terms in the SDE corresponding to the η term in the Fokker-Planck equation could easily be added. This would mean adding a new noise source which would affect the evolution of the position as well as the momentum.

III. APPLICATION OF THE MODEL TO EXPERIMENTAL REGIMES

A. Potentials and heating rates for atomic motion

The "quasiclassical" model discussed in the previous Sec. II can give us a great deal of information about the nature of the dynamics that may be expected in the parameter regimes relevant to the experiments of Hood et al. [7] and Pinkse et al. [8]. In particular we are interested in whether quantization of the cavity field leads to any significant change in the dynamics, in the sense of asking whether the atomic motion is very different in the cavity from what it would be in a free-space standing wave of the same intensity and geometry as the cavity mode. Second, we can investigate the nature of the resulting atomic motion in the cavity field, which can be either predominantly conservative or significantly diffusive and dissipative, depending on the particular parameters of interest.

To obtain a feel for the type of atom dynamics expected, effective potentials and heating rates were calculated for both axial and radial directions of motion. The effective potential of the atom in the cavity field may be calculated from the force by

$$
U(\vec{r}) = -\int_0^{\vec{r}} \vec{F}(\vec{r}')\cdot d\vec{r}'.
$$

The heating rates represent the average increase in the motional energy due to the momentum diffusion at a given position $\vec{r}$, and may be calculated from the diffusion tensor according to

$$\frac{dE}{dt}(\vec{r}) = \mathrm{Tr}[D(\vec{r})]/m.$$

Thus the axial potential at the center of the mode is $U(0,x) = -\int_0^x \vec{F}(0,x')dx'$ and the associated axial heating rate is $dE(0,x)/dt = D_{xx}(0,x)/m$. These quantities along with their radial equivalents $U(\rho,0)$ and $dE(\rho,0)/dt$ are plotted in Fig. 3 for the parameters of Hood et al. [7]. The force and momentum diffusion coefficient for the cavity system were calculated according to the formulas described above by numerical techniques based on Ref. [23]. The field state is expanded in terms of number states, and truncated at an appropriate level and a matrix-continued fraction algorithm is used to calculate D. The axial potentials and heating rates have $\lambda/2 = 426$ nm periodicity inherited from the standing-wave field strength. Observe that the axial heating rates have minima at both field antinodes and field nodes.
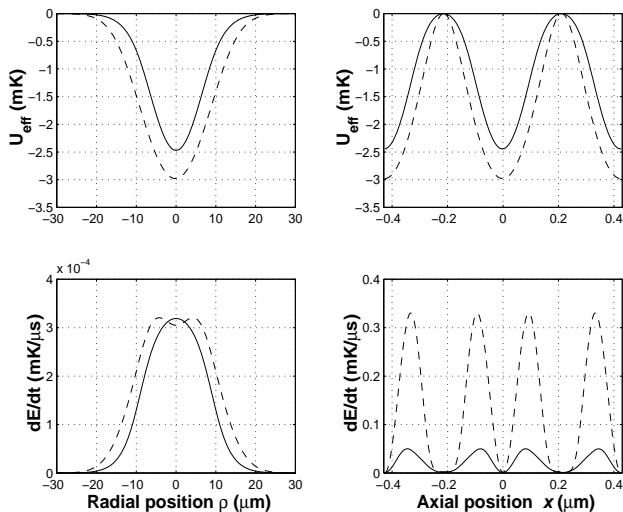

FIG. 3. Effective potentials U_{eff} and heating rates dE/dt in the radial and axial directions for the experiment of Hood et al. (solid traces). The cavity field has a Gaussian waist $w_0 = 14$ μm in the radial direction. The axial standing wave has antinodes at $x = (0, \pm 0.426)\mu m$ and nodes at $x = \pm 0.213\mu m$. All quantities are calculated for $\Delta_{probe}/2\pi = -125$ MHz and $\Delta_{ac}/2\pi = -47$ MHZ, with an empty cavity mean-field strength of $\bar{m} = 0.3$ photons. For comparison, corresponding quantities for an equivalent classical free-space trap are shown as dashed traces. Note that the axial heating in the cavity trap is tenfold smaller, greatly enhancing the trap lifetime.

The first thing to note is that the axial and radial heating rates are very different. In the radial direction, heating is dominated by diffusion due to spontaneous-emission recoils. Axially, however, the reactive or dipole fluctuation component of the diffusion dominates. This

is because the reactive component is proportional to the gradient of the field squared, which is much larger for the axial direction where variations are greater (by a factor of $2\pi w_0/\lambda$). This contribution also has the property that it does not saturate with the atomic response.

It is already clear that it should be possible to trap individual atoms, since the potential depth of roughly 2.5 mK is greater than the initial energy of the atoms in the experiment (around 0.46 mK) and the heating rate in the radial potential is relatively slow. Over 50 μs (a time scale over which the atomic motion is strongly affected by the potential) the total heating will typically still be small compared to the depth of the potential. However, the importance of the quantum character of the relevant fields or phenomena is not ensured by the statement that trapping occurs with a mean field strength of $\bar{m} \sim 1$ photon, since this is trivially the case in an equivalent free-space volume for a field of the same intensity as that inside the cavity.
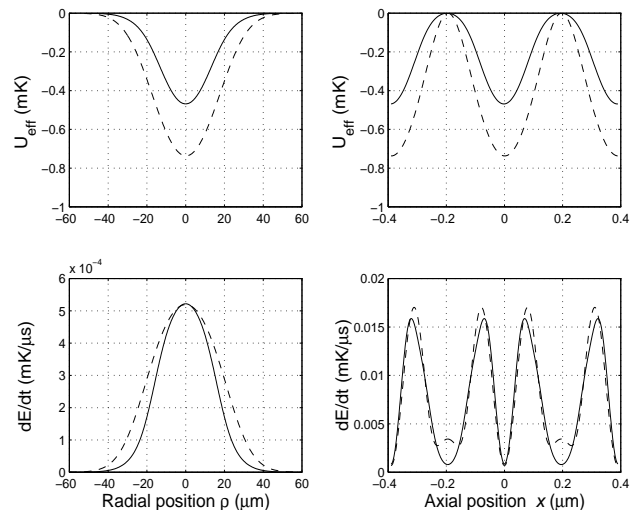

FIG. 4. Effective potentials U_{eff} and heating rates dE/dt in the radial and axial directions for the experiment of Pinkse et al. (solid traces). The cavity field has a Gaussian waist $w_0 = 29$ μm in the radial direction. The axial standing wave has antinodes at $x = (0, \pm 0.390)$ μm and nodes at $x = \pm 0.195$ μm. All quantities are calculated for $\Delta_{probe}/2\pi = -45$ MHz and $\Delta_{ac}/2\pi = -40$ MHz, with an empty cavity photon number $\bar{n} = 0.9$. For comparison, corresponding quantities for an equivalent classical free-space trap are shown as dashed traces. Note that the potential depths and heating rates are comparable in the cavity QED and free-space cases.

In order to see whether a full quantum description of the atom-cavity is necessary in order explain observed effects, Fig. 3 also shows the values calculated for an atom in an equivalent free-space standing wave, calculated by standard techniques [29]. This free-space standing wave has the same geometry as the cavity mode, and the same peak field strength $g_0|\langle a\rangle|^2(0,0)$. The detuning between the free-space field and the atom is chosen to be Δ_{probe}. Perhaps surprisingly, the only large differ-

ence between the two models is in the axial heating rate, where a strong suppression of the axial heating is seen in the quantum calculation. This suppression is an effect of the quantized nature of the intracavity field. The self-consistent coupling of the cavity field and atomic position (in a semiclassical sense) cannot explain this suppression; in fact, by itself this coupling would lead to an increase in diffusion over the free-space case, since the atomic motion within the cavity induces steeper gradients in the field. The suppression of diffusion is then evidence that it is necessary to use a fully quantum description, and speak of single photons rather than classical fields for these experimental parameters. As discussed in Ref. [7], this suppression of the axial heating was essential for the trapping of atoms in the cavity. Thus for these experimental parameters, the eigenvalue structure of Fig. 1 leads to profound differences between the standard theory of laser cooling and trapping and the extension of this theory to the regime of strong coupling in cavity QED.
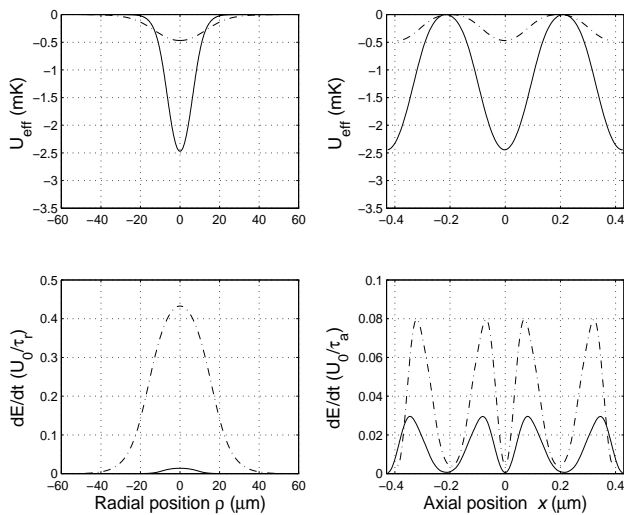

FIG. 5. Comparison of effective potentials and heating rates in the experiments of Hood et al. (solid line) and Pinkse et al. (dash-dotted line). Heating rates are shown in units of trap depths per harmonic oscillation period (in the appropriate trap dimension), providing a direct measure of the degree to which oscillatory motion can be expected to be conservative in nature. Note that differences in w_0 and λ between the two experiments lead to quite different radial widths and slightly different axial periodicities for the quantities plotted.

By way of comparison, the same quantities are plotted for the parameters relevant to Pinkse et al. [8] in Fig. 4. [34]. The smaller value of g_0 in this experiment leads to a smaller effective potential, since the spatial gradients of the dressed state energy levels (which lead to the potential) are proportional to g_0. More importantly, the diffusion values calculated from the full quantum model discussed above are now little different from those of the equivalent free-space standing wave. This lack of a clear difference in potentials or diffusion indicates that the quantized nature of the field is not required to explain

the radial trapping observed in Ref. [8]. Note that the resulting axial heating rates are essentially the same as those of Ref. [7] in absolute magnitude; however, in Ref. [7] the potential was made deeper *without* the expected corresponding increase in diffusion. For the parameters of Ref. [8] one additional interesting feature appears— enhanced cooling of the atom motion relative to the parameters of Ref. [7]. This arises through cavity-mediated cooling [15,16], and as we shall see, has an important effect on the axial dynamics of atoms in the experiment of [8].

We now wish to use these potentials and heating rates to gain an intuitive understanding of the character of atomic motion that we would expect to observe in each case. In particular, we are interested in exploring the degree to which the atomic motion in the potential can be close to conservative motion, or likewise the degree to which it could be dominated by diffusion.

The time scales of relevance to the conservative motion may be characterized by the period associated with small-amplitude oscillations in the bottom of the axial ($\tau_a = 1/f_a$) and radial ($\tau_r = 1/f_r$) potential wells. If the energy changes only by a small fraction (relative to the the total well depth U_0) on this time scale, motion will be nearly conservative. Fig. 5 plots the potentials and heating rates for the two cases in this new set of scaled units; heating rates are expressed as an energy increase per oscillation period, as a fraction of U_0 (note as the atom heats and explores the anharmonicity of the potential, this only lengthens the period of oscillation). Interestingly, we see a clear qualitative difference in the nature of the atomic motional dynamics. For the parameters of Hood et al., in the radial plane spontaneous emission only gives small perturbations to the energy over the time scale of single orbits, and motion is nearly conservative. We note that this low level of diffusion enabled the reconstructions of single-atom trajectories in Ref. [7], for which the small changes in angular momentum could be accurately tracked. A quite different regime is found for the parameters of Pinkse *et al.*, where the radial atomic motion is strongly affected by heating from spontaneous emission kicks. Here an average atom gains an energy of nearly half the well depth in what would be a radial orbit time, adding a large diffusive component to the motion. This same scaling shows that the axial heating rate is also much more rapid on the scale of the potential in Ref. [8], which suggests that the atom will more quickly escape its confinement near an antinode and begin to skip along the standing wave. The qualitative understanding of the atomic motion gained here is borne out by the simulations of Refs. [7] and [8], and is explored in more detail in the simulations to follow.

B. Simulated transits

Simulations of the kind described in Sec. II were performed for the parameters of the two experiments, and individual instances of these simulations give insight into the dynamics of the motion—for example, the relative significance of conservative or dissipative dynamics—and the correlation between atomic motion and the cavity field state, which is in turn measured by detection of the output field. Ensembles of these trajectories provide the statistics of the motion described by the Fokker-Planck equation [Eq. 10] which may then be used to provide histograms of transit times to compare to the experimental data or to test reconstruction algorithms for the motion. In order to approximate the experiment as closely as possible, some effort was made to match the detailed experimental conditions. The two general considerations were to reasonably accurately estimate the initial distribution of atomic positions and momenta for atoms and to consider detection noise and bandwidth when simulating the feedback switching of the probe laser power.

For each trajectory in the simulations, initial atomic position and momentum values were drawn from a probability distribution, which was chosen to correspond to the cloud of atoms following laser cooling and then free fall [7] or launching by an atomic fountain [8] to the cavity mirrors. In the simulations, all the atoms started in a horizontal plane 1 $\frac{3}{4}$ mode waists above or below the center of the cavity mode, where mechanical effects on the atom are negligible. Since the MOT from which the atoms are falling or rising has dimensions much larger than the cavity mode, the initial position in the axial direction was chosen from a flat distribution over the cavity mode, and the initial position along the y axis was also chosen from a flat distribution over 1 $\frac{1}{2}$ mode waists on either side of the mode center—this distance could be modified but atoms that are far out in the mode radially do not typically cause large increases in the cavity transmission, and therefore do not trigger the feedback. The velocity of the atom along the cavity axis is limited by the fact that it must not hit one of the mirrors while falling toward the cavity, and this was also chosen from a flat distribution where the speed was not more than 0.46 cm/s for the cavity of Hood et al. [7]. Although the two experiments have rather different geometries, we estimate that this consideration leads to a very similar limiting velocity for motion along the axis. In the experiment of Pinkse et al. [8], we used 0.4 cm/s. The velocity along the z axis was chosen from a Gaussian distribution appropriate to the temperature of the MOT ($\sim 20\ \mu K$) after polarization gradient cooling. For [7] the velocities in the vertical direction were chosen by calculating as appropriate for an atom falling freely from the MOT (the MOT is situated 3.2mm above the mode with a spatial extent of standard deviation 0.6mm). Thus atoms arriving at the cavity axis have a mean vertical velocity $\bar{v} = 25$cm/s. Some of these parameters such as the height, size and temperature of the initial MOT are not precisely known for the experiment, so that some consideration of the variation of the histograms and other features of the resulting simulations has been made although no systematic optimization in order to obtain the best agreement has been undertaken. In Ref. [8] the mean initial vertical velocity of atoms entering the cavity is 20 cm/s. This speed is very much less than the mean velocity imparted to the atoms by the pushing beam which launches them from the MOT 25 cm below, and as a result the atoms are all near the top of their trajectories. Simple kinematical calculations show that the resulting distribution of velocities should be rather broad compared to the mean. In the absence of more detailed information about the MOT temperature and spatial size and the strength of the pushing beam we choose the initial vertical velocity distribution to be a Gaussian of mean 20 cm/s and standard deviation 10 cm/s—this leads to a distribution of trapping times with a mean that matches the mean reported in Ref. [8]. Each trajectory proceeds until the atom is either a greater radial distance from the center of the mode than it started from, or it has moved sufficiently far in the axial direction that it would hit one of the cavity mirrors.

The detection and triggering are modeled as follows. In the parameter range in which the "quasiclassical" model is valid, the cavity field comes to equilibrium with the atomic position on a time scale much faster than the atomic motion itself, and thus the light transmitted through the cavity (over bandwidths of the order of tens to hundreds of kilohertz) is associated with the atomic motion. At each point in the simulation the intracavity field and intensity expectation values are stored in order to record for each trajectory a noiseless and infinite-bandwidth trace. In practice, experimental traces will look like filtered and noisy versions of these traces. As an atom enters the cavity mode, a weak driving field is present for probing. In order to model the triggering step, the field intensity $\langle a^\dagger a \rangle$ or field amplitude modulus squared $|\langle a \rangle|^2$ is averaged over a time equal to the bandwidth of the detection in the case of heterodyne detection as in Ref. [7], or over the time windows in which photocounts are binned in the case of direct photodetection as in Ref. [8]. A random number with the appropriate variance to represent the shot noise is added and the total is compared with some predecided level—if the transmission exceeds this level the probe laser beam is increased in strength in order to attempt to trap the atom. In the case of Ref. [7] the trigger level is $|\langle a \rangle|^2 = 0.32$, the averaging time is 9 μs, and there is a 2-μs delay between triggering and changing the driving laser power. For the experimental bandwidth of 100 kHz, the appropriate noise has standard deviation 0.05 at a transmitted signal of 0.32. These parameters are chosen so as to match as closely as possible the conditions of the experiment. The same procedure is followed for simulations of the parameters [8]. Although the exact triggering protocol is not described there, we assumed that counts over a period of 10 μs were used to decide whether or not to trigger and

the noise was chosen to be consistent with the reported photon count rate of $2 \times 10^6 \mathrm{s}^{-1}$ [18].

Examples of such trajectories are plotted for the parameters of Ref. [7] in Fig. 6 and for those of Ref. [8] in Fig. 7. The chosen trajectories range in length from the experimentally reported mean transit time upward, and are chosen because they show typical features of the dynamics in each case. It is clear that the two experiments are in quite different parameter regimes, as already indicated by the relative sizes of the potentials and heating rates.

For the parameters of Ref. [7], the atoms orbit in a radial plane; some have nearly circular and some very eccentric orbits. The motion along the axial direction is usually well localized near an antinode of the standing wave, where the axial heating rate is small. This localization occurs because atoms are channeled into the antinodes by the weak potential associated with the initial probing field, which slowly begins to affect an atom as it falls across the mode waist during the detection stage of the experiment. However the strong axial heating that is present away from the antinodes means that once an atom begins to heat axially, it suffers a burst of heating (over several hundred microseconds), which leads to its loss from the potential well associated with a single antinode of the field. Frequently the atom leaves an axial potential well when it is radially far from the center of the cavity mode, since in this case the axial potential becomes weaker. Note that the mean transit time in Ref. [7] corresponds to ~ 3.5 radial orbits around the center of the cavity mode, so transits with multiple oscillations are frequently observed. In Ref. [8] the radial oscillation frequency is slower, so an atom of mean transit time does not in fact make a complete rotation about the mode center. The radial motion in this case is also visibly more stochastic in nature, as a result of the relatively faster spontaneous emission momentum diffusion discussed above.

Another interesting difference between the two parameter regimes is, as suggested in Ref. [8], the relative importance of atomic motion along the standing wave as opposed to oscillations around a single antinode. In the case of Ref. [8], long, strongly trapped transits almost always involve intervals when an atom is skipping along the standing wave, as well as intervals when it is oscillating in an individual well. By contrast, for the parameters of Ref. [7], only a few percent of trajectories involve skipping during times in which the atom is trapped, and this is usually associated with movement over one or two wells with the atom falling back into the adjacent or a nearby well. This happens so quickly that it does not affect the radial motion in practice, or lead to a detectable signal in the output light, so that these rare events of skipping do not affect the reconstructions of Ref. [7].
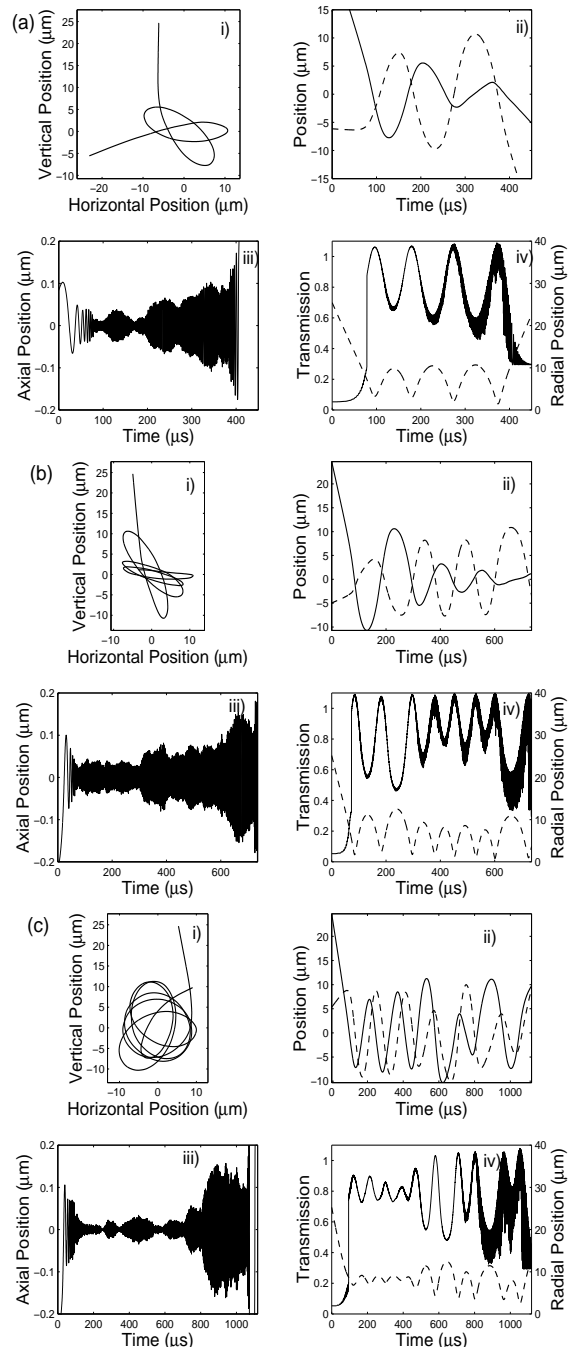

FIG. 6. Typical trajectories from simulations of the experiment of Hood *et al.* as described in the text. The driving parameters are $\Delta_{probe}/2\pi = -125$ MHz and $\Delta_{ac}/2\pi = -47$ MHz, with an empty cavity mean-field strength of $\bar{m} = 0.3$ photons. The trajectories have transit durations of (a) 345 μs, (b) 680 μs, and (c) 1032 μs. This is one, two, and three mean transit times respectively. (i) The radial trajectory of the atom; the z position is plotted against the y position. (ii) The y position (dashed line) and z position (solid line) are plotted as a function of time. (iii) The axial position, where zero is an antinode of the cavity field. (iv) The noiseless infinite-bandwidth transmission $\bar{m}$ (solid line) and the radial distance from the center of the mode (dashed line).
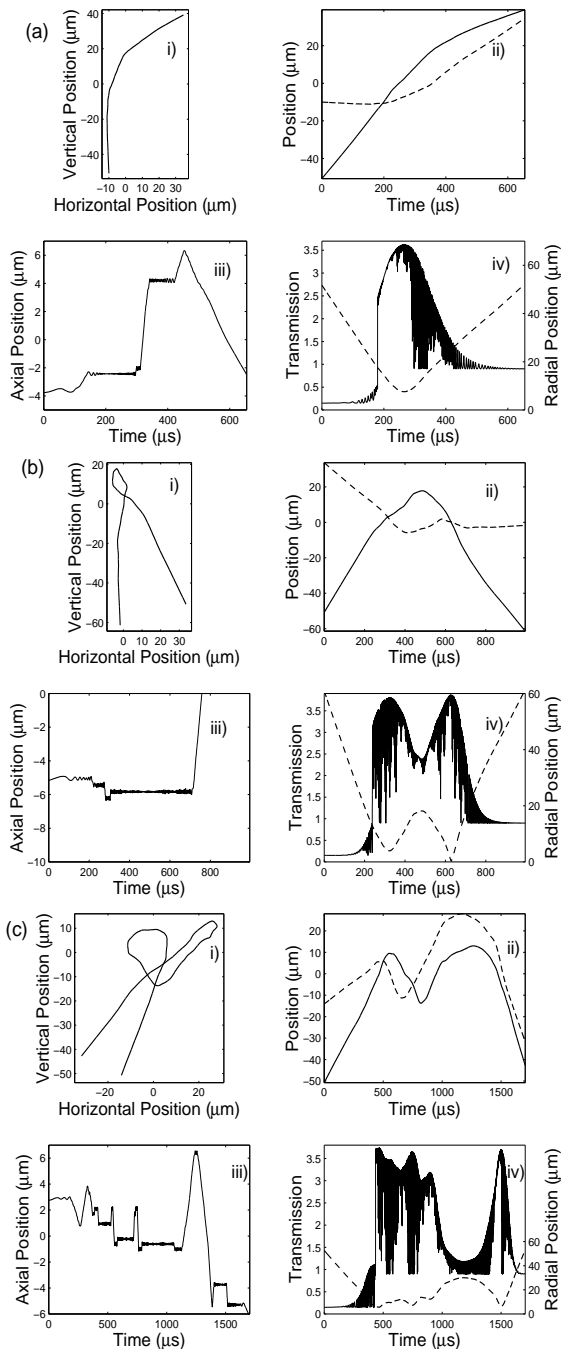
FIG. 7. Typical trajectories from simulations of the experiment of Pinkse *et al.* as described in the text. The driving parameters are $\Delta_{probe}/2\pi = -40$ MHz and $\Delta_{ac}/2\pi = -35$ MHz, with empty cavity photon number $\bar{n} = 0.9$. The trajectories have transit durations of (a) 247 μs, (b) 514 μs, and c) 1358 μs. The experimentally reported mean transit time is 250 μs. (i) The radial trajectory of the atom; the z position is plotted against the y position. (ii) The y position (dashed line) and z position (solid line) are plotted as a function of time. (iii) The axial position, where zero is the mean axial position over the transit. (iv) The noiseless infinite-bandwidth transmission $\bar{n}$ (solid line) and the radial distance from the center of the mode (dashed line).

As noted in Ref. [7], the axial motion often becomes more significant at the end of a transit and as the atom is leaving the mode, which leads to atoms skipping a well in perhaps as many as one in five cases at the end of the transit. We find from the simulations that in Ref. [8], the first escape time from an axial potential well for an atom initially localized near an antinode is sufficiently short compared to the mean trapping time that skipping along the wells almost always takes place. On the other hand, the first escape time is of the order of several times the mean trapping time for the parameters of Ref. [7], so skipping between standing wells is correspondingly rare.

It is interesting to note that the friction coefficient for the parameters of Pinkse *et al.* is much more significant than for the experiment of Hood *et al.*, and plays an important role in the axial motion of the atom. As in the trajectories shown here it is a feature of essentially every trajectory for the parameters of Ref. [8] that the atom spends time in potential wells associated with several different antinodes of the field. However, we performed simulations with the sign of the friction coefficient reversed, and found that no more than a few percent of trajectories were recaptured in a second well after having begun to skip along the standing wave. Clearly the dissipative nature of the motion is an integral feature of the dynamics in this regime, and in particular it enables the atoms to fall back into axial potential wells after escape due to the rapid heating in that dimension.

IV. SIMULATION RESULTS FOR THE EXPERIMENT OF HOOD ET AL.

Having presented the theoretical basis underlying the simulated atom trajectories, in this section we present results of these simulations and their comparison with experimental results as reported in Ref. [7]. We generate a set of simulated trajectories for the parameters $(g_0, \gamma, \kappa) = 2\pi(110, 2.6, 14.2)$ MHz with detuning parameters $\Delta_{ac} = \omega_{cavity} - \omega_{atom} = -2\pi \times 47$ MHz and $\Delta_{probe} = \omega_{probe} - \omega_{atom} = -2\pi \times 125$ MHz. In correspondence with the experimental protocol, the initial pretriggering level of the driving laser gives a 0.05-photon mean-field strength in the empty cavity; when this level rises to 0.32 photons indicating the presence of an atom, we trigger a sixfold increase in the driving strength to a trapping level of a 0.3-photon empty-cavity mean field strength. A close correspondence between theory and experiment is obtained for these results, demonstrating the relevance of this theoretical model to the physics of the actual experiment. In addition, both theoretical and experimental results exhibit features which are relevant to building up a picture of the nature of the single-atom, single-photon trapping and atomic dynamics, both qualitatively and quantitatively.

We begin by presenting the qualitative similarity of experimental and simulated atom transit signals, as observed via detection of cavity transmission as a function

13

of time. Fig. 8 shows two sample experimental transits [(a) and (b)] and two sample simulated transits [(c) and (d)]. For the simulated transits, traces of the corresponding radial and axial motion are also shown. Transmission is shown here as $\bar{m} = |\langle a \rangle|^2$, as is appropriate for the balanced heterodyne detection of Ref. [7]. In the case of the simulated results, the simulated transmission signal has been filtered down to the experimental detection bandwidth of 100 kHz, and both technical noise and shot noise have been added [35]. The transmission signal thus processed can be seen to lose some of the clarity with which it reflects the full atomic dynamics, in comparison to the transmission traces of Fig. 6. In particular, the experimental detection bandwidth is much slower than the time scale for axial oscillation in the confining potential, so that observed transmission signals are averaged over the fast variation in g caused by these axial oscillations. The observed maximum transmission should therefore be lowered relative to theoretical predictions, by an amount dependent on the amplitude of typical axial motion. Thus this finite-bandwidth effect allows for an experimental estimation of the axial confinement of a typical transit. Such a procedure gives an estimate of confinement within ~ 70 nm of an antinode, in good agreement with simulation results which suggest typical confinement within ~ 50 nm. It is important to note that while such tight confinement appears typical over the duration of a trajectory, atoms commonly undergo rapid diffusive heating near the end of their confinement lifetime, which leads to their escape in a majority of cases.

FIG. 8. (a) and (b) Examples of atom transits, i.e., cavity transmission as a function of time as an atom passes through the cavity field for the experiment of Hood et al. Solid traces show atoms trapped using the triggering method described, with an $\bar{m} \simeq 1$ photon peak field strength. For comparison, an untriggered (untrapped) atom transit is shown in the dashed trace. For these traces, the parameters are those of Fig. 3. The empty-cavity 0.3-photon mean-field strength is indicated by the horizontal dashed line. (c) and (d)Theoretical simulation of atom transits for the same Δ_{probe} and Δ_{ac}. Shot noise and technical noise have been added to the transmission signals, which have also been filtered to experimental bandwidth. Other traces show the radial (dashed line) and axial (solid line) motion of the atom. Motion along x, the standing-wave direction, has been multiplied by 10 to be visible on the plot. Note that the atom is very tightly confined in x until rapid heating in this direction causes the atom to escape.

A. Trapping lifetimes

From the entire set of experimental and simulated trajectories like those of Fig. 8, it is possible to investigate some quantitative aspects of the trapping dynamics. First we focus on the trap lifetimes produced by the triggered-trapping scheme. Figures 9(a) and 9(b) show histograms of experimental transit times for un-

trapped atoms and for atoms trapped by means of the triggered-trapping strategy. Transit durations are determined from the experimental data by recording the time interval during which the transmission signal is clearly distinguishable from the empty-cavity transmission level, in the presence of experimental noise. Since the signal-to-noise ratio for observing transits depends on the specific probe parameters, one must be careful to compare untriggered and triggered transits observed with the same detunings and intracavity field strengths. The sole difference must be that in the untriggered case, the empty cavity field is set at a constant strength so that the atom falls through the effective potential, whereas in the triggered case the field begins at a lower level and is only turned up once the atom enters the cavity, thus confining the atom. For example, Fig. 8(a) shows sample untriggered (dashed) and triggered (solid) transit signals which correspond to one another in this way.

In Fig. 9 the difference in transit lifetimes between triggered (b) and untriggered (a) cases is immediately striking. For their initial fall velocity of $\bar{v} = 25$ cm/s, atoms have a free-fall time of ~ 110 μs across the cavity waist $2w_0 = 2(14.06$ μm). As discussed above, the duration of observed transits is limited by the signal-to-noise ratio, which provides a slightly more restrictive cut on transit durations, so the untriggered data set shows a mean duration of 92 μs. In contrast, when the triggered-trapping strategy is employed, the mean trapping lifetime is 340 μs. The dispersion about the mean likewise changes drastically from 75 μs in the untriggered case to 240 μs in the triggered case. These results represent a clear signature of the trapping of single atoms with single photons via this method. In this setting, atoms have been observed to remain trapped in the cavity field for as long as 1.9 ms.

The corresponding theoretical histograms are shown in Figs. 9(c) and 9(d) for the untriggered and triggered cases. The start of the transit is taken to be the time at which an atom could be distinguished in the cavity given the signal to noise, and the final time is taken to be the last point at which the transmission dropped to within the noise of the transmission with no atom. This definition accounts for the fact that as atoms move out in the radial direction the transmission often drops to around the free space value, but returns again to some large value over the time scales of the atomic motion. These levels were chosen to duplicate as closely as possible the protocol for deciding transit times for the experimental data.

The simulated transit set shows a mean trapping time of 96 μs in the untriggered case and 383 μs in the triggered case and dispersions of 84 and 240 μs, respectively. This result is in good agreement with the experimental results when statistical errors and uncertainties in the initial MOT parameters are taken into account. The agreement between experimental and simulated trap lifetimes, in both mean and distribution, gives an indication of the validity of the theoretically calculated trapping potential and diffusive forces on the atom. The 3.5-fold increase

in observed lifetimes due to trapping is made possible by the cavity QED interaction, which allows creation of a deep trapping potential without correspondingly large diffusion as in the free-space case.
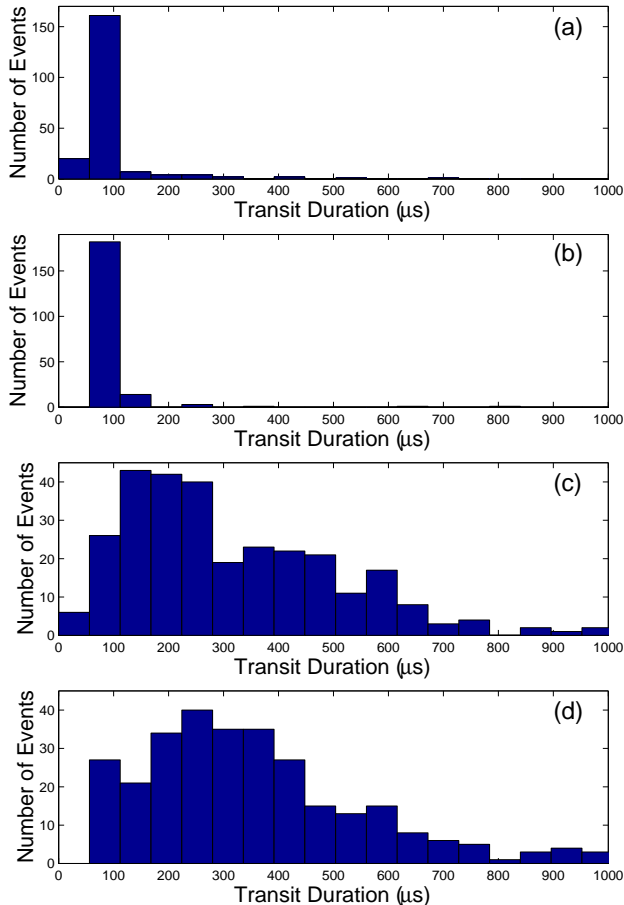

FIG. 9. Observed atomic transit durations for untriggered and triggered cases, with the parameters of Fig. 3. (a) and (c) Experimental data show a mean observation time of 92 μs in the untriggered case (a) and 340 μs in the triggered case (c), indicating the significant trapping effect. For comparison, the free flight time across the cavity waist is 110 μs. (b) and (d) The simulated transit set shows a mean of 96 μs for the untriggered case (b) and 383 μs for the triggered case (d), in good agreement with experiment.

B. Oscillations and radial motion

We now turn to a more detailed investigation of the dynamics of motion experienced by a trapped atom. As we have seen, the transmission signal for a single trapped atom exhibits large variations over time which may be tentatively identified with atomic motion in the radial (Gaussian) dimensions of the cavity field. Thus, for example, the highest transmission occurs when the atom passes closest to the cavity axis, $\rho = 0$. To determine the validity of such an identification, we examine the periods of observed oscillation in the transmission sig-

nal. The calculated effective potential is approximately Gaussian in the radial dimension, so a one-dimensional conservative-motion model predicts periods as a function of oscillation amplitude in this anharmonic effective potential well. Referring to the sample transits of Fig. 8, one does indeed note a trend toward large modulations with long periods and smaller modulations with shorter periods. To quantify this observation, we plot period P versus the amplitude A for individual oscillations, where $A \equiv 2[(H_1 + H_2)/2 - H_c]/(H_1 + H_2)$, with $\{H_1, H_2, H_c\}$ as indicated in Fig. 8.
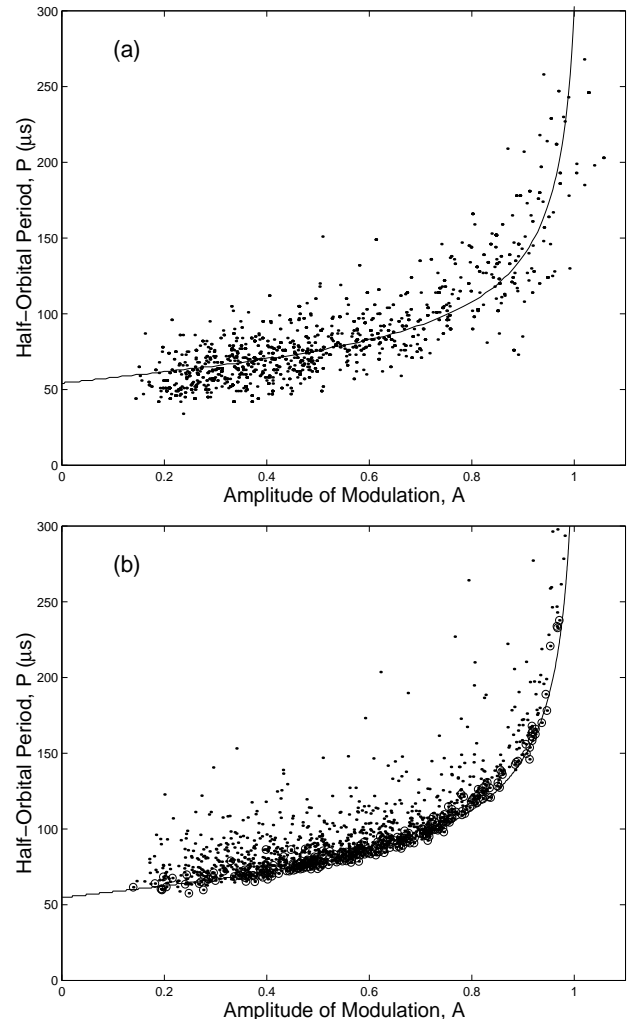

FIG. 10. (a) For experimental transmission data of Hood et al., the modulation period is shown as a function of amplitude. If modulations in transmission are tentatively identified with radial atomic motion, their expected period is half that of the radial motion. The solid curve gives calculated period vs amplitude based on this assumption and on one-dimensional motion in the effective potential $U(\rho, 0)$ of Fig. 3. (b) Corresponding plot for simulated transmission data. Points with lowest underlying atomic angular momentum are plotted with circles; separation by angular momentum reflects the conservative nature of atomic dynamics on time scales comparable to a radial period.

15

Figure 10(a) shows the experimental data plotted along with the calculated curve for one-dimensional motion in the effective potential $U(\rho, 0)$ (see Fig. 3), for the same parameters as Fig. 8. (This is a different data set from that presented in Fig. 4. of Ref [7].) Note that since an atom approaches the cavity axis $\rho = 0$ twice over the course of one orbital period, the predicted period for oscillations in the transmission signal is half the period of the underlying atomic motion. Experimental data clearly map out this calculated curve for radial atomic motion, demonstrating that oscillations in the observed cavity transmission do indeed reflect radial position of an atom as it varies over time within the trap. The agreement also indicates the quantitative correctness of the theoretical model for the radial potential depth and spatial profile. Note that the comparison is absolute with no adjustable parameters.

The same analysis may be performed for transmission oscillations in the set of simulated transits, yielding the plot of Fig. 10(b). This plot again shows agreement with the calculated curve, with some spread away from the line. For simulated transits, it is possible to turn to the underlying atomic position record to determine an angular momentum for the atom during a given oscillation. Thus the oscillation data of Fig. 10(b) are plotted by atomic angular momentum, where lower angular momentum data points are shown with circles. A separation by angular momentum is clearly evident, with lower angular momentum points most closely following the calculated one-dimensional (and thus zero angular momentum) curve. This separation, while it may seem expected, is in fact a non-trivial indication that angular momentum is a valid quantity for the atomic motion over the course of an oscillation period. Since the atomic motion is not in fact conservative, but is also influenced by random (diffusive) forces, a separation by angular momentum can only be expected to occur if the effect of diffusive forces is sufficiently small over the time scale of an orbit in the conservative potential. The plots of Fig. 3 provide an initial indication that this is indeed the case for these parameters, and this idea is borne out by the current investigation. Confidence in the relatively small effect of diffusion over a single orbital period is crucial in the reconstruction of two-dimensional atomic trajectories as in Ref. [7].

V. SIMULATION RESULTS FOR THE EXPERIMENT OF PINKSE ET AL.

Having provided a validation of our capabilities for numerical simulation by way of the results of Sec. IV, we next apply this formalism to the experiment reported in Ref. [8]. At the outset, we note that the various approximations discussed in Sec. II related to the derivation of this quasiclassical model are satisfied to a better degree for this experiment than for the experiment of Ref. [7]. Hence we expect that the correspondence between

the simulations and experiment should be at least of the quality as in the preceding section.

Our starting point is the generation of a large set of simulated trajectories for the parameters reported in Ref. [8], namely, $(g_0, \gamma, \kappa) = 2\pi(16, 3, 1.4)$ MHz with detuning parameters $\Delta_{ac} = \omega_{cavity} - \omega_{atom} = -2\pi \times 35$ MHz and $\Delta_{probe} = \omega_{probe} - \omega_{atom} = -2\pi \times 40$ MHz. The initial pretriggering level of the driving laser gives a 0.15-photon mean intensity in the empty cavity; when this level rises to 0.85 photons, indicating the presence of an atom, we trigger an increase in the driving strength to a trapping level of 0.9-photon empty-cavity intensity. These criteria are intended to follow the parameters indicated in Figs. 2 and 3 of Ref. [8]. Note that for the cavity geometry of this experiment, the time for an atom to transit freely through the cavity mode in the absence of any light forces is $\tau_0 = 2w_0/\bar{v} = 290$ μs, where as before we take twice the cavity waist w_0 as a measure of the transverse dimension of the cavity.

A. Histograms of transit durations

From the set of such simulated trajectories (~ 400 in this particular case), we can construct histograms for the number of events as a function of total transit signal duration. Following the experimental protocol of Ref. [8], which employed photon counting, we base this analysis upon the intracavity photon number $\bar{n} = \langle a^\dagger a \rangle$ rather than $|\langle a \rangle|^2$ as in Ref. [7], although this distinction is not critical to any of the following considerations.
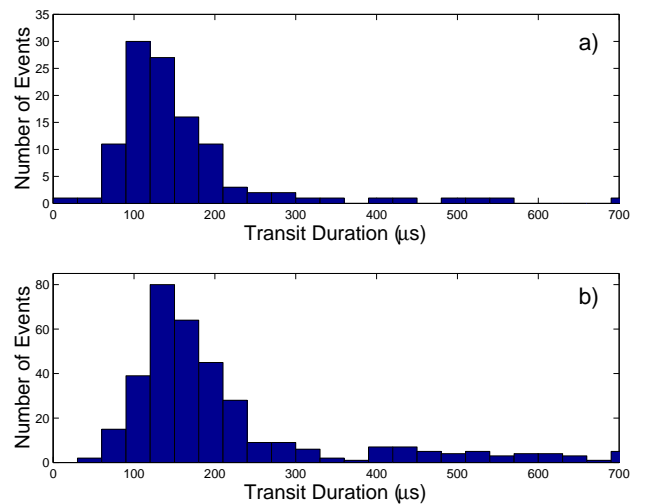

FIG. 11. Simulated atomic transit durations for untriggered and triggered cases, with the parameters of Pinkse et al., as in Fig. 7. (a) The untriggered transit set shows a mean observation time of 160 μs. (b) The triggered transit set shows mean duration 280 μs, in good agreement with the experimentally quoted mean of 250±50μs. For comparison, free-fall time across the cavity waist is 290 μs.

The resulting histograms for the experiment of Ref. [8] are displayed in Fig. 11 for the cases of untriggered and triggered trajectories. As in the discussion of Fig. 9, the external drive strengths are set to be equal for this comparison to provide equal detectability for an atom passing through the cavity mode. Detection with lower external drive strength gives a lower signal-to-noise ratio for atom detection, which results in detected transit durations much shorter than the actual passage time through the cavity (which is of order $\tau_0 = 2w_0/\bar{v}$), as for example in Fig. 2(a) of Ref. [8].

In support of the validity of our simulations for the experiment of Pinkse et al. (including the initial atomic velocity and position distribution and the triggering conditions), note that the mean of 280 μs for the histogram in the triggered case of Fig. 11(b) corresponds quite well with that quoted in Ref. [8], namely, $\bar{\tau}_{\mathrm{exp}} = 250 \pm 50$ μs. Further, the histograms in Fig. 11 exhibit an extension of the mean transit duration from 160 μs for the case of no triggering in (a) to 280 μs with triggering in (b), in support of the claim of trapping in Ref. [8]. The dispersion of events around the mean is quite large in both cases, 161 μs in the untriggered set and 282 μs in the triggered set. The increase in the mean is largely associated with an increase in the number of events in the range 200-300 μs, as well as in the number of rare events much longer than the mean duration. Once again we note that the dissipative nature of the dynamics plays a crucial role in the observed motion for the experiment of Pinkse et al. A histogram of transit durations calculated with the sign of the friction coefficient reversed has a lower mean than that of transits with no triggering.

However, it is certainly worth noting that the observed "average trapping time" $\bar{\tau}_{\mathrm{exp}} = 250 \pm 50$ μs quoted in Ref. [8], as well as the corresponding mean time from our simulations, are smaller than the time $\tau_0 = 290$ μs for an atom to transit freely through the cavity mode. Additionally, even in the case of no triggering, there is already a significant number of events with similar long duration to those in (b) with triggering. Such events arise from the relatively large contribution of diffusion-driven fluctuations whereby an atom randomly loses a large fraction of its initial kinetic energy as it enters the cavity. That such fluctuations play a critical role should already be clear from the plots of the confining potentials and diffusion coefficients in Fig. 4.

B. Radial motion

Trapping dynamics can also be explored if atomic oscillation in the trapping potential can be directly observed. Certainly the observations presented in Fig. 10 make this case for the experiment of Ref. [7], with the observed oscillation frequencies found to be in good quantitative agreement with those computed directly from the anharmonic potential without adjustable parameters and with

the results of the numerical simulations.

Towards the goal of constructing a similar plot for the parameters of Ref. [8], consider a long-duration transit event such as that in Fig. 7(c). Recall that the output flux from the cavity is given by the cavity decay rate $2\kappa_d$ into the relevant detection channel times the intracavity photon number, or $I = 2\kappa_d\bar{n} = 2\kappa_d\langle a^\dagger a\rangle$, with then the detected count rate found from the overall propagation and detection efficiency as $R = \xi I$. Of course, in any actual experiment the full information displayed for the intracavity photon number $\bar{n}$ is not available because of finite detection efficiencies ($\xi < 1$) and the requirement to average over many cavity lifetimes in order to achieve an acceptable signal-to-noise ratio (roughly for a time such that $\sqrt{R\delta t} \gg 1$).
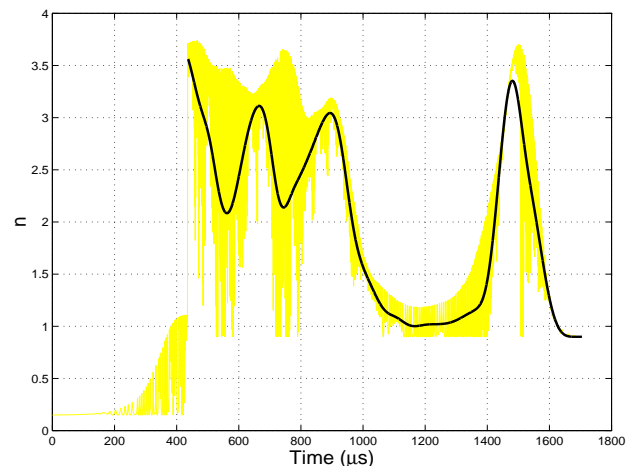

FIG. 12. Transmission data for the simulated transit of Fig. 7(c). The full ideal signal $\bar{n}(t)$, with infinite bandwidth and no degradation due to cavity escape efficiency or subsequent system losses, is shown in gray. Slow variations are caused by radial motion while fast variations reflect axial motion. The black trace results from applying to this ideal signal a low-pass filter with cutoff $f_c = 10$ kHz intended to optimize the visibility of any radial oscillations for frequencies $f \lesssim 5$ kHz, where $f_0^{(r)} = 2.6$ kHz is the orbital frequency for small-amplitude oscillation near the bottom of the radial potential. The resulting filtered transmission signal shows variations due to both radial motion and axial heating.

Rather than attempt a detailed analysis of such effects for the experiment of Ref. [8], here we wish to illustrate several generic effects that hinder definitive observation of radial oscillations in this regime. We therefore take *the full ideal signal $\bar{n}(t)$ with no degradation due to cavity escape efficiency or subsequent system losses* (which we estimate to be $\kappa_d/\kappa \sim 0.17$ and $\xi \sim 0.6$ for an overall efficiency of 0.11). As shown in Fig. 12, to this ideal signal we apply a low-pass filter with cutoff $f_c = 10$ kHz intended to optimize the visibility of any radial oscillations for frequencies $f \lesssim 5$ kHz, where $f_0^{(r)} = 2.6$ kHz is the orbital frequency for small-amplitude oscillation near the bottom of the radial potential. As before, recall that

a periodic variation in the radial coordinate at frequency f results in a variation in $\bar{n}$ at $2f$. Precisely such a filtering protocol was implemented for the analysis in Fig. 10, there with $f_c = 25$ kHz in correspondence to the larger radial oscillation frequencies ($f_0^{(r)} = 9.4$ kHz for Ref. [7]) [36].

Not surprisingly, the frequent and large bursts of axial heating evident for the simulated trajectories of Fig. 7 result in large variations in the intracavity photon number on time scales set by twice the axial oscillation frequency $f_0^{(a)} \approx 430$ kHz. While these axial oscillations cannot be directly resolved in the detected counting signal $R(t)$, their envelope nonetheless leads to variations in $\bar{n}(t)$ and hence $R(t)$ on time scales comparable to that associated with radial motion (i.e., $1/2f_0^{(r)}$), as is apparent in Fig. 12. Consequently, the low-pass filtering [or, equivalently, the time averaging over segments in $R(t)$] that is required experimentally to obtain an acceptable signal-to-noise ratio gives rise to observed variations in $\bar{n}(t)$ that can arise from either axial or radial atomic motion. In the particular transit shown in Fig. 12, two apparent variations on time scales $\simeq 200$ μs are introduced by a filtering of the axial motion, whereas the longer modulation ($\simeq 600-\mu$s duration) does reflect the radial position of the atom. This is something of a generic feature of the several hundred simulated transits examined; shorter-time-scale modulations ($\lesssim 300$ μs) can reflect either a genuine radial excursion or a filtering of axial motion, whereas very long period variations (500–600 μs) are indicative of radial atomic motions. This simply reflects the fact that the bursts of axial motion tend to have time scales limited to a few 100 μs.

To illustrate these points further, we have constructed a plot of period versus normalized amplitude of transmission oscillations from our simulations of the experiment of Pinkse et al. [8], with the result given in Fig. 13. We emphasize that the protocol followed is precisely as for the analysis that led to Fig. 10(b) for the experiment of Hood et al. [7] (see also Fig. 4 of Ref. [7]), with the exception of the aforementioned reduction in the low-pass cutoff frequency. In marked contrast to that case, here there is a poor correspondence between the distribution of orbital periods from the ensemble of simulated trajectories and the prediction from the potential obtained from Eq. (9). Referring to the discussion of Fig. 12 above, we note that about 2/3 of the points in the 100–300 μs range result from averaging over axial motion, whereas for longer-period (P¿300 μs) modulations, 80% of the observed points reflect changes in the radial motion, but with associated transmission amplitude typically modified by the presence of axial motion. The results of Fig. 13 [which are for the ideal case of $\bar{n}(t)$ without signal degradation due to finite escape and detection efficiency] suggest that only in restricted cases can temporal variations in $R(t)$ be attributed to radial motion, and not instead of (or in addition to) the envelopes of axial heating processes. Indeed, such effects are well known in the literature, having been previously discussed for the case of individual atoms falling through the cavity mode (albeit without triggering or trapping) [21,17]. A similar conclusion was reached, namely, that axial heating processes contaminate the frequency band associated with radial motion, thereby precluding inferences about radial motion. For the data presented by Pinkse et al. [8], the long ($\simeq 500$ μs) time scale of the modulations suggests an assignment of these signals to radial motion; however, a more detailed characterization of the atom dynamics over a larger ensemble of transits should yield this more definitively.

It is also worth noting that the quoted average trapping time $\bar{\tau}_{\exp} = 250 \pm 50$ μs in Ref. [8] is itself less than $1/f_0^{(r)} = 390$ μs, which is *shortest time* for a full radial orbit. Hence any conclusion about motion in the radial plane must necessarily be based upon rare events in the tail of the histograms of Fig. 11. The rare occurrence of these long events is reflected in the small number of data points in Fig. 13, which was constructed from the same number of simulated transits as Fig. 10(b).
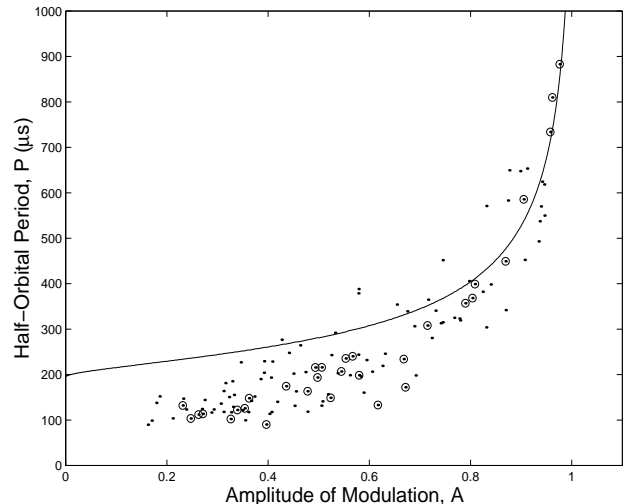

FIG. 13. For simulated transmission data corresponding to the parameters of Pinkse et al., the modulation period is shown as a function of amplitude. If modulations in transmission are tentatively identified with radial atomic motion, their expected period is half that of the radial motion. The solid curve gives calculated period vs amplitude based on this assumption and on one-dimensional motion in the effective potential $U(\rho, 0)$ as in Fig. 4. Points with lowest underlying atomic angular momentum are plotted with circles. Lack of separation by angular momentum reflects the diffusive nature of atomic dynamics on time scales comparable to or shorter than one radial period.

C. Axial Motion

We next turn to analyze motion along the axial direction, and to the statement of Pinkse et al. [8] that Fig. 4 of Ref. [8] "is direct evidence for the atom moving

along the cavity axis," as opposed to instances of localization around an antinode for which "hardly any periodic structure is visible." In their analysis, Pinkse et al. employed a function $g^{(4)}(\epsilon, \tau, \epsilon)$, whose intention is to pick out two-time correlations in intensity, with an enhanced signal-to-noise ratio of intensity fluctuations by measuring coincidences of photon pairs. Here we attempt to investigate manifestations of the axial motion independent of the details of any specific such function by analyzing $\bar{n}(t)$ directly by way of a windowed fast-Fourier transform (FFT). More specifically, for each trajectory from a large ensemble from our simulations, we apply a FFT to the record $\bar{n}(t)$ with a Hanning window centered at time t_i and of total width 25 μs, with the window then offset sequentially to $t_{i+1} = t_i + 5$ μs to cover the whole range of a given atomic trajectory. The window width 25 μs is chosen to be in close correspondence to the record length of 20 μs employed by Pinkse et al. Longer window widths do not qualitatively change the results of our analysis, while a substantially shorter-duration window leads to a loss of requisite frequency resolution.

Two examples from an extended set of such transforms are given in Figs. 14 and 15. Parts (a) of each of these figures show the mean intracavity photon number $\bar{n}(t)$, the axial coordinate $x(t)$, and a contour plot of the windowed FFT $\mathcal{N}_{t_i}(\Omega)$ for a single atomic trajectory for the parameters of Ref. [8]. Here $\mathcal{N}_{t_i}(\Omega)$ is the windowed FFT of $\bar{n}(t)$ over the entire duration of the trajectory, with $t_i = t_0 + i \times 5$ μs. Parts (b) of Figs. 14 and 15 compare $\mathcal{N}_{t_i}(\Omega)$ for two particular values of t_i, namely, at a time t_{flight} corresponding to the midst of a flight of the atom over several antinodes of the intracavity standing wave (i.e., variations in axial coordinate x by several units of $1\lambda/2$) and at a time $t_{localized}$ for which there is appreciable heating along the axial direction but for which there is no flight (i.e., the atom remains localized within the same axial well). The times $(t_{flight}, t_{localized})$ are indicated by the arrows in the top two panels of parts (a).

Perhaps the most striking aspect of the comparison of the spectral distributions $\{\mathcal{N}_{flight}(\Omega), \mathcal{N}_{localized}(\Omega)\}$ for the cases with and without flight is their remarkable similarity [in (b) of Figs. 14 and 15]. Both display prominent peaks near $\Omega_p/2\pi = f_p \simeq 500$–600 kHz, which is in accord with the expected frequency for large-amplitude oscillation in the axial potential, for which the harmonic frequency $f_0^{(a)} \approx 430$ kHz (recall that frequency of atomic dynamics is half the frequency of the associated variations in $\bar{n}(t)$). This result is also in accord with that from Fig. 4(b) of Pinkse et al., for which their simulation leads to $1/\tau_p \simeq 550$ kHz for variations in the function $g^{(4)}$.

However, our analysis, as in the comparison of $\{\mathcal{N}_{flight}(\Omega), \mathcal{N}_{localized}(\Omega)\}$ above, indicates that neither the observation of a peak in $\mathcal{N}(\Omega)$ around Ω_p nor of oscillatory structure in $g^{(4)}(\epsilon, \tau, \epsilon)$ around $\tau_p \simeq 2\pi/\Omega_p$ is sufficient to justify direct evidence for the atom moving along the cavity axis. Rather, peaks in $\mathcal{N}_{t_i}(\Omega)$ are ubiquitous around frequencies $\Omega_p/2\pi \simeq 500$–600, and ap-

pear whether the atom's motion is localized (but heated) within a given axial well or whether the atom is in flight across several wells. This feature follows from an analysis of the full record of $\bar{n}(t)$ without the deleterious effects of finite escape and detection efficiency, or of finite detection bandwidth. Such a result suggests that the measurements of Fig. 4 in Ref [8] are not in and of themselves sufficient to establish unambiguous observation of atomic motion across several wells of the cavity field standing wave.
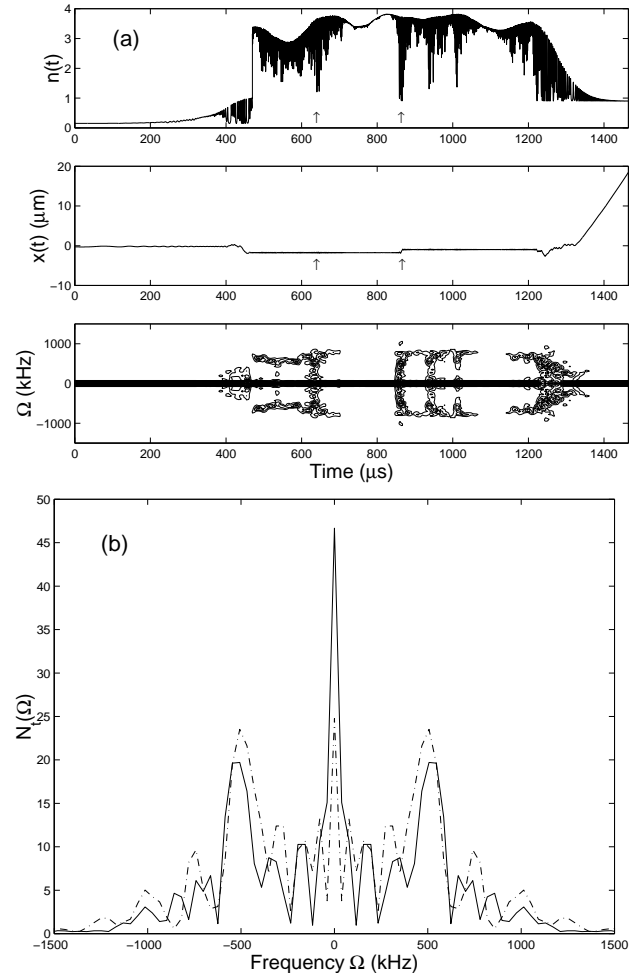

FIG. 14. (a) Mean intracavity photon number $\bar{n}(t)$, axial position $x(t)$, and a contour plot of the modulus of the windowed FFT $\mathcal{N}_t(\Omega)$ of $\bar{n}(t)$ for a simulated transit for the parameters of Pinkse et al. (b) At the times indicated in (a), $|\mathcal{N}_{localized}(\Omega)|$ is plotted corresponding to the arrow at $t_{localized} = 652$ μs (solid curve) and $|\mathcal{N}_{flight}(\Omega)|$ corresponding to the arrow at $t_{flight} = 867$ μs (dash-dotted curve). There are apparently only minor differences between these two spectra, which does not support the conclusion about axial motion drawn from Fig. 4 in Ref. [8].

Our analysis does suggest that it may still be possible to distinguish between axial motion confined within a well and flight along the cavity axis through a more careful quantitative analysis of the respective spectral

19

distributions $\{\mathcal{N}_{flight}(\Omega), \mathcal{N}_{localized}(\Omega)\}$. With reference to Figs. 14 and 15, note that a principal distinction between these cases is that in the case of flight there is a large *decrease* of spectral content in the lowest frequency components around $\Omega = 0$. This decrease reflects the fact that axial skipping causes full-range variation in g, and thereby pulls down the time-averaged value of transmission $\bar{n}(t)$. In addition, we note an *increase* in $\mathcal{N}_{flight}(\Omega)$ as compared to $\mathcal{N}_{localized}(\Omega)$ for Fourier components in a broad range around $\Omega_p/2$ and up to Ω_p. The increase appears to reflect atomic motion that, during skipping, explores the full nonlinear (anharmonic) range of the axial potential. These characteristics of the overall spectral distributions seem to discriminate more reliably between flight and localized heating than does a single-frequency peak criterion; they may still offer an avenue for observing atomic skips across the standing wave.
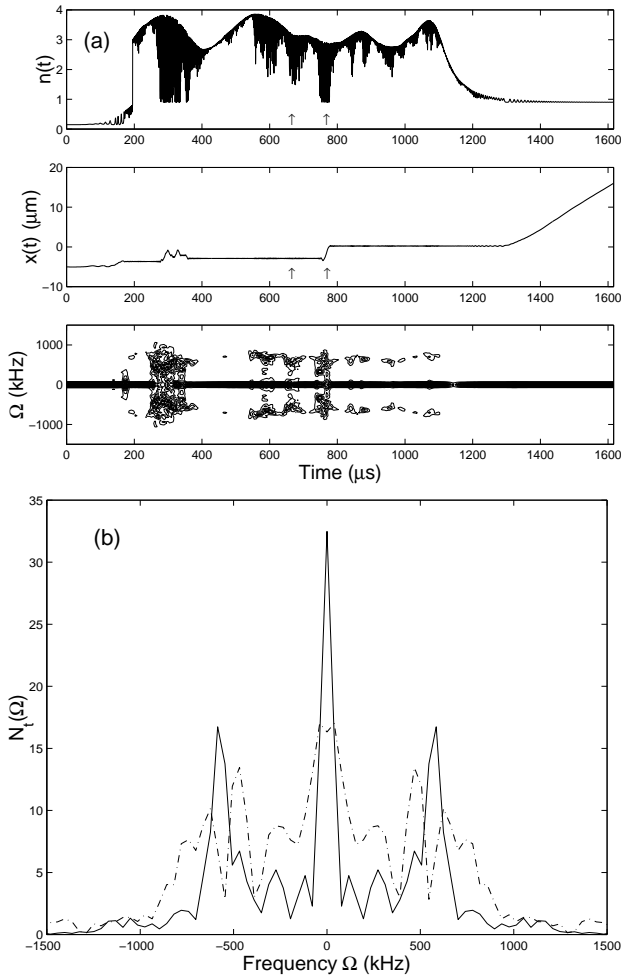

FIG. 15. (a) Mean intracavity photon number $\bar{n}(t)$, axial position $x(t)$, and a contour plot of the modulus of the windowed FFT $\mathcal{N}_t(\Omega)$ of $\bar{n}(t)$ for a simulated transit for the parameters of Pinkse et al. (b) At the times indicated in (a), $|\mathcal{N}_{localized}(\Omega)|$ is plotted corresponding to the arrow at $t_{localized} = 673$ μs (solid curve) and $|\mathcal{N}_{flight}(\Omega)|$ corresponding to the arrow at $t_{flight} = 780$ μs (dash-dotted curve). See the text for discussion.

VI. CONCLUSIONS

A principal objective of this paper has been to investigate the extent to which light-induced forces in cavity QED are distinct from their free-space counterparts. Our perspective has been to seek qualitatively new manifestations of optical forces at the single-photon level within the setting of cavity QED. Note that the importance of a quantum character for the relevant fields or phenomena is not ensured by the statement that the mean photon number $\bar{n} \sim 1$, since this is trivially the case in an equivalent free-space volume for a field of the same intensity as that inside the cavity.

As a starting point, we have presented comparisons between the effective potential $U_{eff}(\rho, x)$ in cavity QED and the corresponding free-space potential, as well as of the diffusion coefficients in both contexts (Figs. 3 and 4). Perhaps surprisingly, even in a regime of strong coupling as in Ref. [8], there are only small differences between the cavity QED and free-space potentials and diffusion coefficients. Note that the comparison of Fig. 4 includes "the back action of the atom on the cavity field" [8], and yet there are nonetheless no substantive differences between the cavity QED and free-space cases for the experiment of Pinkse et al. Hence, although the cavity QED interactions do bring a substantial advantage for atomic detection within the cavity volume, we conclude that the claim of trapping an atom with single photons in Ref. [8] involves no new characteristics unique to the cavity QED environment, with the conservative forces and diffusion largely described by the well-known free-space theory (Fig. 4). Friction which enhances trapping in this regime can be ascribed to cavity-mediated cooling effects [15,16], which are in themselves not uniquely features of the quantized-field treatment. However, more analysis is required to determine if the observed effects of friction do indeed rely on the cavity-field quantization.

By contrast, for the experiment of Hood et al., a comparison of the free-space theory and its cavity QED counterpart demonstrates that the usual fluctuations associated with the dipole force along the standing wave are suppressed by an order of magnitude. A semiclassical treatment of the cavity field yields large diffusions like those calculated for the free-space trap. Indeed, if it were not for the reduction of heating in the quantized cavity QED case, an atom would be trapped for less than the period of a single radial orbit before being heated out of the well for the parameters of Ref. [7]. Our calculations support the conclusion that the suppression in dipole-force heating is based upon the Jaynes-Cummings ladder of eigenstates for the atom-cavity system, which to our knowledge represents qualitatively new physics for optical forces at the single-photon level within the setting of cavity QED.

In terms of a more complete analysis, the effective potential $U_{eff}(\rho, x)$ and the diffusion coefficient $D(\rho, x)$ are

important ingredients in the quasiclassical theory that we have developed for atomic motion in cavity QED. By way of detailed, quantitative comparisons with the experiment of Hood et al. in Sec. IV, we have validated the accuracy and utility of our numerical simulations based upon the quasiclassical theory. As part of this comparison, we have demonstrated agreement between experiment and simulation for histograms of the duration of transit events, with mean $\bar{\tau}_t = 340$ μs for the histogram in the triggered case of Fig. 9b extended well beyond the mean $\bar{\tau}_u = 92$ μs for the untriggered case. Furthermore, $\bar{\tau}_t$ exceeds the transit time $\tau_0 = 110$ μs for an atom to transit freely through the cavity mode. The simulated trajectories of Fig. 6 together with the comparison of Fig. 10 for the experiment of Hood et al. strongly support the conclusion that atomic motion is largely conservative in nature, with only smaller contributions from fluctuating and velocity-dependent forces. Atomic motion is predominantly in radial orbits transverse to the cavity axis. The (suppressed) axial heating is important, but only towards the end of a given trajectory leading to ejection from the trap. Knowledge of the time dependence $\rho(t)$ for the radial coordinate (by way of the detected field emerging from the cavity and the solution of the master equation) as well of the confining potential $U(\rho, 0)$ allow an algorithm to be implemented for inference of the actual atomic trajectory, as demonstrated in Ref. [7] and discussed in greater detail in Ref. [37].

In the case of Ref. [8], numerical simulations for the parameters appropriate to this experiment lead to histograms with mean 280 μs in the triggered case of Fig. 11(a) and 160 μs for the untriggered case of Fig. 11(b), which should be compared to the time $\tau_0 = 290$ μs for an atom to transit freely through the cavity mode in this experiment. The simulated transits of Fig. 7 indicate that atomic motion in this case is dominated by diffusion-driven fluctuations in both the radial and axial dimensions with friction playing an important role in the axial direction. The character of the motion hampers inference of atomic motion from the record of intracavity photon number. Axial heating leads to repeated large bursts of axial excursions during an atomic transit, and hence to large oscillations in the intracavity photon number $\bar{n}(t)$. The envelopes of these oscillations have appreciable Fourier content in the range of interest for observation of radial motion, so that there is not an unambiguous signature for the radial motion in the record of $\bar{n}(t)$ on short time scales, such as those presented in Ref. [8]. Similarly, the result by Pinkse et al. for hopping or flights over the antinodes of the cavity standing wave is not substantiated by a closer inspection of the Fourier content of the relevant signals. As documented in Figs. 14 and 15, similar signals can be observed for an atom localized (but heated) within a single standing-wave well. We emphasize that these conclusions concerning the work of Ref. [8] are based upon the analysis of several hundred simulated trajectories, apparently well beyond the few cases presented in that paper.

Beyond these comments directed to the prior work of Refs. [7,8], we suggest that the capability for numerical simulation of the quasiclassical model of atom motion in cavity QED should have diverse applications. For example, we are currently applying the simulations to the problem of feedback control of atomic motion. Given the capability to infer an atomic trajectory in real time, it should be possible to apply active feedback to cool the motion to the bottom of the effective potential $U_{eff}(\vec{r})$.

ACKNOWLEDGMENTS

[1] *Cavity Quantum Electrodynamics, Advances in Atomic, Molecular and Optical Physics, Supplement 2*, edited by P. Berman (Academic, New York, 1994).

[2] For a more recent review, see contributions in the special issue of Physica Scripta **T76**, 1–234 (1998).

[3] H. J. Kimble, Phys. Scr. **T76**, 127 (1998).

[4] C. J. Hood, M. S. Chapman, T. W. Lynn, and H. J. Kimble, Phys. Rev. Lett. **80**, 4157 (1998).

[5] J. Ye, C. J. Hood, T. Lynn, H. Mabuchi, D. W. Vernooy, and H. J. Kimble, IEEE Trans. Instrum. Meas. **48**, 608 (1999).

[6] P. Münstermann, T. Fischer, P. Maunz, P. W. H. Pinkse, and G. Rempe, Phys. Rev. Lett. **82**, 3791 (1999).

[7] C. J. Hood, T. W. Lynn, A. C. Doherty, A. S. Parkins, and H. J. Kimble, Science **287**, 1447 (2000).

[8] P. W. H. Pinkse, T. Fischer, P. Maunz, and G. Rempe, Nature **404**, 365 (2000).

[9] P. Münstermann, T. Fischer, P. Maunz, P. W. H. Pinkse, and G. Rempe, Phys. Rev. Lett. **84**, 4068 (2000).

[10] S. Haroche, M. Brune, and J. M. Raimond, Europhys. Lett. **14**, 19 (1991).

[11] B.-G. Englert, J. Schwinger, A. O. Barut, and M. O. Scully, Europhys. Lett. **14**, 25 (1991).

[12] H. Mabuchi, Q. A. Turchette, M. S. Chapman, and H. J. Kimble, Opt. Lett. **21**, 1393 (1996).

[13] A. S. Parkins, in *International Quantum Electronics Conference*, 1996 OSA Technical Digest Series (Optical Society of America, Washington D. C., 1996) p26.

[14] J. Dalibard and C. Cohen-Tannoudji, J. Phys. B **18**, 1661 (1985).

[15] P. Horak, G. Hechenblaikner, K. M. Gheri, H. Stecher, and H. Ritsch, Phys. Rev. Lett. **79**, 4974 (1997).

[16] V. Vuletić and S. Chu, Phys. Rev. Lett. **84**, 3787 (2000).

[17] H. Mabuchi, J. Ye, and H. J. Kimble, Appl. Phys. B: Lasers Opt. **68**, 1095 (1999).

[18] P. Münstermann, T. Fischer, P. W. H. Pinkse, and G. Rempe, Opt. Commun. **159**, 63 (1999).

[19] A. S. Parkins and R. Müller, J. Mod. Opt **43**, 2553 (1996).

[20] H. Mabuchi, Phys. Rev. A **58,** 123 (1998).

[21] A. C. Doherty, A. S. Parkins, S. M. Tan, and D. F. Walls, Phys. Rev. A **56**, 833 (1997).

[22] G. Hechenblaikner, M. Gangl, P. Horak, and H. Risch, Phys. Rev. A **58**, 3030 (1998).

[23] S. M. Tan, J. Opt B: Quantum Semiclass. Opt. **1**, 424 (1999).

[24] T. W. Mossberg, M. Lewenstein, and D. J. Gauthier, Phys. Rev. Lett. **67**, 1723 (1991).

[25] M. Lewenstein and L. Roso, Phys. Rev. A **47**, 3385 (1993).

[26] D. W. Vernooy and H. J. Kimble, Phys. Rev. A **56**, 4287 (1997).

[27] H. Carmichael, *An Open Systems Approach to Quantum Optics* (Springer-Verlag, Berlin, 1993).

[28] J. Javanainen and S. Stenholm, Appl. Phys. **21**, 35 (1980).

[29] C. Cohen-Tannoudji, in *Fundamental Systems in Quantum Optics, Les Houches, Session LIII, 1990*, edited by J. Dalibard, J. M. Raimond, and J. Zinn-Justin (Elsevier, Amsterdam, 1992), pp. 1–164.

[30] K. Berg-Sorensen, Y. Castin, E. Bonderup, and K. Molmer, J. Phys. B **25**, 4195 (1992).

[31] G. S. Agarwal and K. Molmer, Phys. Rev. A **47**, 5158 (1993).

[32] C. W. Gardiner, *Handbook of Stochastic Methods for Physics, Chemistry and the Natural Sciences*, 2nd ed. (Springer-Verlag, Berlin, 1985).

[33] W. H. Press, S. A. Teukolsky, W. T. Vetterling, and B. P. Flannery, *Numerical Recipes in C: The Art of Scientific Computing*, 2nd ed. (Cambridge University Press, Cambridge, 1992).

[34] For the experiment of Ref. [8], the free-space standing wave for comparison is assigned the same peak intensity $g_0\langle a^\dagger a\rangle(0,0)$ as the cavity field mode. The use of peak $\langle a^\dagger a\rangle$ in this case vs peak $|\langle a\rangle|^2$ in the case of Ref. [7] reflects the fact that photon counting was employed in Ref. [8], while detection was via heterodyne in Ref. [7].

[35] Technical noise arises from imperfections in the cavity lock (in particular, a mechanical resonance in the cavity mount at 60 kHz), and contributes a signal $\simeq$50–100 % of the shot noise rms amplitude.

[36] A digital filter is employed, using the built-in Matlab Butterworth filter routine butter[5,0.01] for the simulations of Hood *et al.* [Fig. 10(b)], and butter[3,0.004] for the simulations of Pinkse et al. (Fig. 13). In each case, the first parameter refers to the order of the filter, and the second to the cutoff frequency as a fraction of the Nyquist frequency (a sample rate of 0.2 μs was used in the simulations.) In each case, parameters are chosen in an attempt to optimally extract information about radial oscillations from the transmission signal. The filter cutoff chosen for the Pinkse et al. simulations was the lowest that could still track genuine radial motion of an atom passing through the cavity.

[37] A. C. Doherty, T. W. Lynn, R. J. Legere, and H. J. Kimble, in preparation.

This figure "figure2.gif" is available in "gif" format from:

http://arXiv.org/ps/quant-ph/0006015v4

This figure "figure8.gif" is available in "gif" format from:

http://arXiv.org/ps/quant-ph/0006015v4